The mechanics of shallow magma reservoir outgassing.

A. Parmigiani[1], W Degruyter[2], S. Leclaire[3,4], C. Huber[5] and O. Bachmann[1]

[1]Institute of Geochemistry and Petrology, ETH Zurich, Clausiusstrasse 25, 8092 Zurich, Switzerland.
[2]School of Earth and Ocean Sciences, Cardiff University, Main Building, Park Place, Cardiff, CF10 3AT, Wales, UK
[3]Computer Science Department, University of Geneva, Route de Drize 7, 1227 Carouge, Switzerland
[4]Department of Chemical Engineering, Polytechnique Montréal, 2500, Chemin de Polytechnique, Montreal, H3T 1J4, Canada
[5]Department of Earth, Environmental and Planetary Sciences, Brown University, Rhode Island 02912, USA

Corresponding author: Andrea Parmigiani (andrea.parmigiani@erdw.ethz.ch)

Key Points:

- Outgassing potential of a magma reservoir is a strong function of its crystal content.
- Outgassing efficiency is also modulated by mechanical coupling between reservoir and crust.
- Simulations that consider both aspects reveal that the majority of exsolved volatiles is released at intermediate to high crystallinity.

Abstract

Magma degassing fundamentally controls the Earth's volatile cycles. The large amount of gas expelled into the atmosphere during volcanic eruptions (i.e. volcanic outgassing) is the most obvious display of magmatic volatile release. However, owing to the large intrusive:extrusive ratio, and considering the paucity of volatiles left in intrusive rocks after final solidification, volcanic outgassing likely constitutes only a small fraction of the overall mass of magmatic volatiles released to the Earth's surface. Therefore, as most magmas stall on their way to the surface, outgassing of uneruptible, crystal-rich magma storage regions will play a dominant role in closing the balance of volatile element cycling between the mantle and the surface. We use a numerical approach to study the migration of a magmatic volatile phase (MVP) in crystal-rich magma bodies ("mush zones") at the pore-scale. Our results suggest that buoyancy driven outgassing is efficient over crystal volume fractions between 0.4 and 0.7 (for mm-sized crystals). We parameterize our pore-scale results for MVP migration in a thermo-mechanical magma reservoir model to study outgassing under dynamical conditions where cooling controls the evolution of the proportion of crystal, gas and melt phases and to investigate the role of the reservoir size and the temperature-dependent visco-elastic response of the crust on outgassing efficiency. We find that buoyancy-driven outgassing allows for a maximum of 40-50 % volatiles to leave the reservoir over the 0.4-0.7 crystal volume fractions, implying that a significant amount of outgassing must occur at high crystal content (>0.7) through veining and/or capillary fracturing.

Index Terms and Keywords (up to 5):

Magma reservoirs outgassing, gas migration in mushes, multiscale modeling of magma reservoirs, Earth's volatile cycle.

Introduction

On Earth, magmatic processes control the exchange of volatile species (H_2O, CO_2, S, Cl, F, Li, B, noble gases …) between the mantle and the atmosphere. The volatiles are initially dissolved in silicate melts produced in the upper mantle. As magmas ascend to shallower levels and undergo crystallization, a low viscosity and low density Magmatic Volatile Phase (hereafter MVP) can exsolve. The various processes that govern the transport and extraction of the MVP, as it leaves its shallow magmatic hearth and reaches the surface, remain a major challenge to our understanding of volatile cycling between the mantle and the surface.

Magma outgassing at shallow reservoir storage depth, here referred to as *intrusive outgassing*, is likely to be dominant over gas release through volcanic eruptions, here referred to as *volcanic outgassing*, as (1) plutonic rocks are typically dry (<1 wt.% H_2O when fully solid [*Caricchi and Blundy*, 2015; *Parmigiani et al.*, 2014; *Whitney*, 1988]), and (2) most of the magma stalls in the crust (intrusive:extrusive ratio between 10:1 and >30:1 in most arc settings [*Lipman and Bachmann*, 2015; *Ward et al.*, 2014; *White et al.*, 2006]). The amount of volatiles expelled during volcanic eruptions can be spectacular [*Iacovino et al.*, 2016; *Soden et al.*, 2002; *Vidal et al.*, 2016; *Westrich and Gerlach*, 1992], but is likely to constitute only a small fraction of the overall mass budget. *Shinohara* [2013] estimated a global budget of volatile release of volcanic centers in Japan over the last ~40 years to which explosive eruptions only contributed less than 15%, supporting the idea that volcanic eruptions do not provide the largest share of volatiles to the atmosphere at subduction zones. Hence, gaining insights into the physical and chemical processes regulating outgassing in shallow magma reservoirs is not only a crucial piece of the puzzle for constraining the state of magmas stalling in the Earth's crust [e.g., *Anderson et al.*, 1984; *Boudreau*, 2016; *Huber et al.*, 2010; *Mungall*, 2015; *Pistone et al.*, 2015; *Sisson and Bacon*, 1999], but it is also fundamental to volatile cycling and ore formation [*Candela*, 1991; *Chelle-Michou et al.*, 2017; *Gerlach*, 1991; *Heinrich and Candela*, 2012; *Huybers and Langmuir*, 2009; *Shinohara*, 2008; *Sillitoe*, 2010; *Wallace*, 2005; *Weis et al.*, 2012; *Zellmer et al.*, 2015].

Volatile exsolution is largely controlled by the pressure-temperature evolution of magmas in the crust. Magma reservoirs are known to build incrementally over time [*Annen et al.*, 2006; *Gelman et al.*, 2013; *Karakas and Dufek*, 2015; *Karakas et al.*, 2017; *Lipman*, 2007; *Menand et al.*, 2015; *Miller et al.*, 2011], and spend most of their supra-solidus life at high crystallinity (i.e. mush state [*Bachmann and Bergantz*, 2008; *Cooper and Kent*, 2014; *Huber et al.*, 2009; *Lee and Morton*, 2015; *Marsh*, 1981]). In arcs, magmas are commonly volatile-rich (i.e. > 4 wt.% H_2O [*Blundy et al.*, 2010; *Plank et al.*, 2013]) and are expected to reach a high volume fraction of MVP in mush zones in the upper crust (upon significant crystallization of mostly anhydrous phases). Such conditions set the stage for efficient MVP mobility through the upper part of the magmatic column [*Candela*, 1994; 1997; *Huber et al.*, 2010; *Parmigiani et al.*, 2014; *Parmigiani et al.*, 2016].

At high MVP and average crystal volume fractions, crystal confinement tends to favor MVP migration [*Huber et al.*, 2010; *Oppenheimer et al.*, 2015; *Parmigiani et al.*, 2011; *Parmigiani et al.*, 2016; *Spina et al.*, 2016] by promoting the formation of continuous and elongated MVP fingers, which serve as preferential outgassing pathways [*Parmigiani et al.*, 2014; *Parmigiani et al.*, 2016]. Additionally, an increase in melt segregation rate due to bubble growth ("gas filter-pressing" [*Pistone et al.*, 2015; *Sisson and Bacon*, 1999]), compaction, and melt buoyancy induced by a growing suspended MVP volume fraction [*Boudreau*, 2016], may favor the simultaneous physical segregation of melt and bubbles from the crystal-rich environment. This process may favor the extraction of eruptible high-SiO_2 rhyolite lenses and aplite-pegmatite bodies through an extended MVP-generated micro-fracture (veins) network [*Pistone et al.*, 2015; *Weinberg*, 1999].

In this study, we investigate shallow magma reservoir outgassing by coupling a pore-scale hydrodynamics study of MVP fingers formation to a magma reservoir scale model (Fig. 1). The pore-scale simulations focus on the competition between buoyancy and capillary stresses that takes place at the pore-scale and its effect on outgassing in rheologically-locked crystal-rich magma storage regions. We constrain the critical MVP volume fraction ε_g^{cr} that is needed for MVP migration by fingering to take place. These pore-scale simulations illustrate the complex multiphase fluid dynamics that govern the transport of MVP. As such, the pore-scale simulations provide an upper bound for the outgassing efficiency by considering that transport is the limiting factor. However, other thermo-mechanical feedbacks may control outgassing at the reservoir scale. Hence, we introduce the pore-scale results as a parameterization into a magma reservoir model to further test the impact of reservoir size, the temperature-dependent visco-elastic response of the surrounding crust on outgassing efficiency, as well as the effect of transient cooling and crystallization on gas exsolution and migration.

2. MVP mobility at the pore-scale: the competition between buoyancy and capillary stresses.

To model the MVP migration at the pore scale we make the following assumptions:

1. the timescale for MVP exsolution by crystallization ("second boiling") is longer than the time for the MVP to potentially establish flow pathways (if they occur),
2. pore-scale pressurization due to volatile exsolution is limited and likely efficiently dissipated through the permeable mush,
3. the crystal framework remains static (no deformation) over the time required for the MVP to migrate through the domain [*Parmigiani et al.*, 2016],
4. due to the limited vertical extent of our pore-scale sample volume (~ few cubic centimeters), the ambient (lithostatic) pressure is uniform,

5. although Fe-Ti oxides and sulfide phases are potential nucleation sites for bubbles [*Edmonds et al.*, 2015; *Gardner and Denis*, 2004; *Navon and Lyakhovsky*, 1998], they are by far volumetrically secondary to other non-wetting mineral phases such as plagioclase. Therefore, we consider MVP as non-wetting [*Huber et al.*, 2010; *Huber et al.*, 2012; *Parmigiani et al.*, 2014].

The mode of MVP transport discussed here will be referred to as hydrodynamic migration (also known as "capillary invasion"), and it is expected to be efficient as long as the effective permeability for the MVP does not allow for significant overpressure to build up locally at the pore scale. Our pore-scale calculations focus on this regime. However, for large crystal volume fraction (>~70 vol.%) and/or small average crystal size (lower pore-to-pore connectivity), the capillary resistance to bubble migration will become significant. Hence, in natural environments, local pressurization can potentially occur. Initially, such local pressurization, together with bubbles hydrostatic pressure drop, can allow elongated bubbles (or slugs) to overwhelm the capillary entry pressure of adjacent throats and drive bubble/slug migration in a capillary invasion mode. However, when significant local pressurization builds up, a second, brittle, mode of MVP migration can be expected in crystal-rich magmas, referred to as "capillary fracturing" [*Holtzman et al.*, 2012; *Oppenheimer et al.*, 2015]. Contrary to capillary invasion, capillary fracturing implies that the bubble excess pressure exceeds both the confining stress and the frictional resistance of the crystalline medium, inducing matrix deformation, crystal displacement (i.e. frictional sliding) [*Shin and Santamarina*, 2010] and eventually bubble migration.

In the present study, we assume the crystalline matrix in the mush to resist frictional sliding. Crystal matrix deformation due to MVP displacement is therefore not taken into account in our pore-scale calculations. This assumption is valid in crystal-rich magmas where the crystal volume fraction is above the critical random packing threshold (i.e. for crystal volume fraction ~0.4), especially if we assume the mush to be coarse-grained (mm-sized crystals) and consider a high confining pressure P_c (~1-2.5 kbars). We estimate the crystal size D_c for which the transition from capillary invasion to capillary fracturing would occur using the scaling law $D_c \sim (\sigma/\mu_f)P_c^{(-1)}$ [as in *Eriksen et al.*, 2015; *Holtzman et al.*, 2012] where σ and μ_f are the interfacial tension between the two immiscible fluids and the friction coefficient between crystals, respectively. In this context, the throat size is a proxy for crystal size since the throat size scales with both decreasing crystal size and/or increasing crystal volume fraction. The interfacial tension between an H_2O-dominated MVP and melt is σ = 0.07-0.1 N/m [*Mangan and Sisson*, 2005]. To our knowledge, the friction coefficient in a connected crystal framework remains poorly constrained; however, it is most likely not negligible as crystals have angular shapes and rough surfaces, which promote interlocking. Choosing $\mu_f \sim 0.2$ as a lower bound (i.e. steel balls particle-particle friction coefficient [*Li et al.*, 2005]) and a confining pressure P_c ~1-2.5 kbars yields a D_c on the order of nanometers. This scaling argument suggests that at intermediate crystal volume fraction (e.g. $0.4<\varepsilon_x<0.7$), where pore-to-pore connectivity remains significant, MVP migration is within the regime of capillary invasion. At higher crystal volume fraction, instead, when the pore-to-pore connectivity is low (throat size on the order of nanometers), capillary fracturing under shallow magmatic conditions can become the dominant mode for MVP transport. Recent laboratory experiments of bubble growth in silicate crystal-rich magmas with ~100 micrometer average crystal size seem to support the idea that fractures only occur at $\varepsilon_x>0.75$ [*Pistone et al.*, 2015].

In the hydrodynamics migration regime, the competition between buoyancy and capillary stresses on MVP bubbles can be described by the Bond number (Bo):

$$Bo = \frac{\Delta\rho g D^2}{\sigma}$$

where $\Delta\rho$ is the density difference between the melt and MVP bubbles, g is the acceleration due to gravity, D the bubble diameter and σ the interfacial tension. We estimate Bo values to lie between 0.1-1 for medium to coarse grained crystal mushes with an average crystal size of ~3-5 mm [*Bachmann and Bergantz*, 2004], using σ=0.07 N/m ($0.024< \sigma <0.1$ N/m, *Hammer* [2004]) and $\Delta\rho$=2000 kg/m^3. Because of slow exsolution and limited pressure build-up, we assume the bubble diameter D to be equal to the average pore diameter D_{pc} of the crystalline environment. Heterogeneity in the crystal size and shape can sensibly affect the packing, making the estimation of D_{pc} for natural environments difficult [*Barker and Mehta*, 1992]. However, for the sake of our Bo estimates, we set the ratio between pore diameter and grain diameter to that found in randomly packed beds of spheres (0.2-0.4 at the random packing threshold value) [*Barker and Mehta*, 1992; *Hinedi et al.*, 1997]; when using an average crystal size of 3-5 mm, D_{pc} is therefore in the range ~0.6-2 mm.

We investigate MVP transport at the pore-scale by performing immiscible two-phase lattice Boltzmann (LB) simulations (see pore-scale inset in Fig. 1 and Appendix A for more information about the LB algorithm adopted for our investigation). We conduct our simulations in rigid crystalline matrices with variable crystal volume fractions (see Fig. 2).

The size of the crystalline domain is set to 160x160x240 grid points. Crystal sizes vary between ~10 and ~30 grid points. We first compute the intrinsic permeability of each medium with a single fluid transport model (e.g. Fig. 2e-f) [*Degruyter et al.*, 2010] and, scale up the results considering an average crystal size of 4 mm [*Cheadle et al.*, 2004] (see Fig. 2g).

Our simulation domains have periodic boundary conditions in all spatial directions and no-slip internal boundary conditions (bounce-back scheme [*Chopard et al.*, 2002]) on the crystal surfaces. The pore space is occupied by either a low density, low viscosity non-wetting fluid or a more viscous wetting fluid, which represent the MVP and melt phase, respectively. The MVP is fully non-wetting (contact angle 180°), where the wettability is set following the approach of *Leclaire et al.*, 2016. The viscosity ratio between the melt and the MVP is set to 100, which is well under the real value but large enough to reproduce the correct stress balance on bubbles [*Parmigiani et al.*, 2016]. The Reynolds number of our pore-scale calculation is small for both early stages (i.e. while bubbles interacts to form channels Re < 1) and MVP transport through channels (Re ~ 1). In our pore-scale simulations, various values for the Bond number are set by varying the magnitude of the buoyancy force acting on the vapor phase [*Ngachin et al.*, 2015; *Parmigiani et al.*, 2011; *Ren et al.*, 2016].

In order to mimic the initial spatial distribution of MVP associated with second boiling, we distribute MVP bubbles with different radii randomly inside the crystalline matrix (Fig. 3). The whole set of parameters explored with our calculations is reported in Appendix A, Table 1. During the early stages of each simulation, bubbles sitting next to each other (e.g. in the same pore or very well connected pores) can coalesce and form larger bubbles; this occurs in particular at high bubble and crystal volume fractions (see Fig. 3).

3. Results

3.1. Window of optimal outgassing efficiency

We seek to determine the MVP volume fraction (ε_g) threshold at which connected MVP channels can form (Fig.4a-b). Above the threshold, outgassing will be efficient, as it significantly decreases the rate of energy dissipation during MVP migration [*Parmigiani et al.*, 2016] (see Fig.4c and Fig.4d). We study the onset of dynamic MVP percolation over a range of MVP (ε_g) and crystal (ε_x) volume fractions (i.e. $0.03 \leq \varepsilon_g \leq 0.19$ and $0.4 \leq \varepsilon_x \leq 0.75$) that are characteristic of isobaric (at ~2 kbars) degassing for intermediate arc magmas (with ~4-7 wt.% H_2O). The dashed lines in Fig. 4e&f are MVP volume fraction for closed-system degassing calculated with *rhyolite-MELTS [Gualda et al., 2012]*. We also consider three Bo number values (Bo=0.1, 0.5, 1) to estimate the effect of the crystal/pore sizes on the capillary resistive stresses exerted by the crystalline environment on bubble mobility.

Our results demonstrate that the competition between the positive effect of crystal confinement on MVP channel formation and the capillary resistance to bubble mobility controls the critical MVP volume fraction ε_g^{cr} at which fingering pathways of MVP form and sustain. ε_g^{cr} is therefore a function of the crystal volume fraction ε_x (see Fig. 4e&f). The first effect, crystal confinement, promotes more efficient outgassing by enhancing bubble coalescence, deformation and migration, which ultimately favor channel formation and stability [*Parmigiani et al.*, 2016]. The effect of crystal confinement on MVP migration is clearly observed in Fig. 4b where it results in a negative $\partial\varepsilon_g^{cr}/\partial\varepsilon_x$ (Fig. 4e for Bo=0.5) up to $\varepsilon_x \simeq 0.5$. For larger crystal volume fractions ($\varepsilon_x > 0.5$), $\partial\varepsilon_g^{cr}/\partial\varepsilon_x$ becomes positive and is associated with the increasing capillary resistance to MVP migration as the mean pore throat diameter decreases. At high crystallinity (ε_x>0.6 for Bo=0.5 and ε_x>0.7 for Bo=1), we observe a shift in behavior, with MVP migration by fingering becoming inefficient (Fig. 4e&f). This effect is enhanced when the crystal size is small (ε_x>0.5 at Bo=0.1, Fig. 4f) and/or the crystal content becomes very high (as shown by the positive correlation between ε_g^{cr} and ε_x in Fig. 4e&f).

Overall, we find a favorable crystallinity window (between $0.4 \leq \varepsilon_x \leq 0.7$ over $0.1 \leq \mathrm{Bo} \leq 1$), where the combination of crystal confinement and limited capillary resistance allows for MVP channel formation and optimal MVP migration. Our results suggest that at Bo=0.5 and ε_x>0.7, connected MVP channels do not form unless almost half of the pore-space is occupied by MVP, conditions that have been suggested to be favorable to the formation of percolation pathways strictly based on static-geometrical percolations arguments [*Candela*, 1994]. However, our calculations show that the strong non-wettability of the MVP impedes the formation of percolating pathways unless bubbles are able to overcome the capillary resistivity of the porous medium (bottlenecks in throats). We generally find that for ε_x>0.7 and/or Bo<1, additional processes such as pore-pressure build-up by compaction [*Boudreau*, 2016] or bubble overpressure are required to initiate bubble migration, and eventually, when pore connectivity is strongly reduced, by capillary fracturing [*Holtzman et al.*, 2012].

The formation and destruction of MVP channels control outgassing in crystallizing magma bodies. MVP transport through channels is likely to be intermittent in magmatic environments [*Candela*, 1994] since, in order to be stable, channels require an adequate volatile flux [*Stöhr and Khalili*, 2006] that a magmatic source can sustain only for a limited time [*Candela*, 1994; 1997]. Therefore, MVP channels are bound to pinch off, stopping efficient outgassing, and leaving behind a trail of capillary trapped bubbles or slow moving MVP fingers (MVP residual saturation). Such capillary-trapped bubbles will however participate to the formation of new channels if additional MVP is injected or exsolved into the system.

3.2. 2nd boiling vs. injection from below.

The critical MVP volume fraction for MVP channel formation ε_g^{cr} (deduced from our pore-scale simulations) depends on the mode of volatile delivery to the crystalline mush zone. When the MVP is injected from below (Fig. 5a), as would be expected if a deeper section of the magmatic system is undergoing significant degassing [*Parmigiani et al.*, 2014], ε_g^{cr} is a monotonous function of ε_x and decreases with ε_x as would be expected for 2-phase percolation governed by crystal confinement (Fig. 5b). In contrast, simulations initiated with a random spatial distribution of bubbles (2nd boiling) require more MVP to reach a similar degree of outgassing (Fig. 6-7). This difference is due to the MVP invasion process selecting only the most efficient flow pathways in the scenario with MVP injection from below. In contrast, the random distribution of MVP during 2nd boiling leads to a significant fraction of bubbles trapped in poorly connected pores, which do not contribute to the overall MVP flux. The difference in critical MVP volume fraction between 2nd boiling and injection from below provides, therefore, a way to quantify the volume of MVP that remains trapped in the porous medium after 2nd boiling until other processes such as capillary fracturing [*Holtzman et al.*, 2012] or gas-filter pressing [*Pistone et al.*, 2015] take place.

3.3 Outgassing parameterization

We now wish to describe the efficiency of outgassing at the spatial and temporal scales of the magma reservoir and test the effect of thermomechanical processes on outgassing dynamics. To this end, we will couple the results of the pore-scale simulations with a reservoir scale model using a parametrized approach. We build a pore-scale parameterization for Bo=0.5 that describes MVP channel formation and enhanced outgassing by estimating (1) the critical MVP volume fraction needed for channel formation (from Fig. 4e) and, once channels are formed, (2) the intrinsic (single-phase) permeability k of the porous medium (Fig. 2g), and (3) the MVP relative permeability of the mush k_r (Fig. 8). We retrieve the relative permeability for the MVP by calculating the MVP discharge through the crystalline medium (Fig. 8).

Although our results also indicate an increase in relative permeability with increasing MVP volume fraction (for $\varepsilon_g > \varepsilon_g^{cr}$), reflecting the ability to form more than one connected MVP finger through the porous network or improving MVP channels connectivity, only k_r estimated at the onset of MVP channel formation for each explored crystal volume fraction is used for the parameterization. When migration becomes efficient with respect to exsolution, the MVP volume fraction is bound to remain close to ε_g^{cr}. Due to the positive effect of solid confinement on MVP channel formation and outgassing, we observe a non-linear increase in MVP discharge and relative permeability with increasing crystal volume fraction, with a maximum value around ε_x=0.5. We find that the MVP discharge can vary by three orders of magnitude between $0.4<\varepsilon_x<0.7$.

For Bo=0.5 and crystal volume fraction between 0.4 and 0.7, our pore scale simulations yield the following relationship between the critical MVP volume fraction and the crystal volume fraction (Fig. 4e-f):

$$\varepsilon_g^{cr} = 2.75\varepsilon_X^3 - 2.79\varepsilon_X^2 + 0.6345\varepsilon_X + 0.0997 \qquad (1).$$

Similarly, we find the following correlation between the intrinsic permeability and the crystal volume fraction:

$$k = 10^{-4}(-0.0534\varepsilon_X^3 - 0.1083\varepsilon_X^2 - 0.0747\varepsilon_X + 0.0176)\ m^2 \qquad (2).$$

Finally, our calculations lead to the following expression for the relative permeability as a function of the crystal volume fraction:

$$k_r = -2.1778\varepsilon_X^4 + 5.1511\varepsilon_X^3 - 4.5199\varepsilon_X^2 + 1.7385\varepsilon_X - 0.2461 \qquad (3).$$

4. Coupling the pore-scale dynamics with a large-scale thermo-mechanical magma reservoir model

We implement the pore MVP migration parameterization of Eqs 1-3 (see Fig. 9) in a reservoir-scale model [*Degruyter and Huber*, 2014; *Degruyter et al.*, 2016] to provide quantitative estimates of the proportion of volatiles exiting the reservoir over various ranges of crystal content during the cooling of a shallow magma reservoir. Our goal is to assess the importance of factors that cannot be considered explicitly in the pore-scale simulations (e.g., reservoir size, temperature and rheology of the wall-rocks) as well as transient cooling, which controls the temporal evolution of the relative proportions of the three phases in the magma reservoir (melt, crystals and exsolved volatiles).

The thermo-mechanical evolution of the magma reservoir is solved with a lumped parameter approach (see Appendix B). We consider an initially mobile (crystal volume fraction <0.4) 3-phase magma volume, which we refer to as the magma chamber, that sits in a colder visco-elastic shell (a crystal mush that gradually transitions into the surrounding crust). The magma chamber is considered homogeneous, which allows tracking the evolution of the average volume fraction and density of the melt, crystals and MVP. The different phases are assumed to be in equilibrium. We further track the changes in pressure, temperature, and volume of the magma chamber. For this study, we consider the scenario of a monotonously cooling magma chamber at 2 kbar that crystallizes and exsolves a MVP and 2nd boiling is therefore the only source of MVP.

Natural subvolcanic magma reservoirs are likely to be not as homogeneous as assumed in our model. Heterogeneities (particularly in crystal content (see Fig. 1); e.g., *Bachmann and Bergantz* [2004]; *Gutierrez et al.* [2013]; *Hildreth* [2004]; *Marsh* [1989]) may influence channels formation, either enhancing (in the most crystalline parts) or decreasing (in crystal-poor regions) MVP bubbles connectivity [*Parmigiani et al.*, 2016]). However, we note that magmas are likely to be dominantly stored as fairly homogeneous crystal mushes [*Huber et al.*, 2009], and the volumes of crystal-poor regions, potentially storing volatiles (decreasing outgassing), are limited with respect to the overall bulk mush; therefore, the outgassing efficiency predicted by our volume-averaged approach should be relatively robust.

5. Thermo-mechanical reservoir model: results

We performed two sets of magma reservoir simulations to focus on the effects of (1) temperature dependent rheology of the crust (visco-elastic crust with a far-field temperature of 250 and 300 °C, respectively) and (2) the size of the chamber, on outgassing (initial size of the chamber from 5-500 km^3). The temporal evolution of the crystal content for each of these simulations is reported in Fig.10, where time is normalized by the cooling time scale $\tau_c = R^2/\kappa$, with R the initial radius of the reservoir and κ the thermal diffusivity of the crust (Table 2). Since the crystal content for each of the two tested scenarios follows a very similar temporal trend (Fig.11 & 12), we can describe (1) the total volatile mass fraction evolution, (2) the volatile mass fraction loss, (3) the overpressure of the reservoir and (4) the MVP volume fraction evolution as a function of crystal volume fraction.

We find that outgassing is limited by the availability of MVP (as in the pore-scale simulations, i.e., saturation-limited) in large magma reservoirs hosted within a hot and compliant crust (Fig. 1 (a); Fig. 11 & Fig. 12). This is because the decompression of the reservoir caused by the loss of MVP is damped by the viscous relaxation of the surrounding crust; the pressure in the reservoir therefore remains near lithostatic and prevents the development of significant adverse pressure gradients that would impede outgassing. A colder crust and/or smaller reservoir, on the other hand (Fig.1 (b); Fig.11 & Fig.12), responds mostly elastically to the volume loss associated with outgassing, which mechanically hinders the efficiency of the outgassing process as pressure gradients oppose the migration of the MVP out of the reservoir.

A hot crust and large reservoir are most favorable for outgassing. Under these conditions, our model shows that the magma with an initial water content of 5.5 wt.% can lose up to ~40 % of its original water content before reaching $\varepsilon_x \cong 0.7$ (total water content after outgassing from MVP channels decreases to 3.25 wt.%, see Fig. 11a&c). Such value is clearly dependent on the choice of Bo number value (here Bo=0.5), initial water content (here 5.5 wt.% H2O), and reservoir depth (2 kbars ~ 8-10 km depth). Higher initial water content, shallower storage levels and larger crystal/pore sizes would enhance the amount of water released before the capillary fracturing stage.

Nonetheless, our calculations show that a substantial amount of volatiles remain trapped by capillary forces above ε_x>0.7. As plutons have a residual volatile content typically <1 wt.% [*Caricchi and Blundy*, 2015; *Whitney*, 1988], the remaining MVP must ultimately escape the cooling reservoirs by alternative processes such as gas-filter pressing [*Pistone et al.*, 2015; *Sisson and Bacon*, 1999] and capillary fracturing [*Holtzman et al.*, 2012; *Shin and Santamarina*, 2010] that are not taken into account into our pore-scale parametrization. These processes likely enhance the extraction of the melt-MVP mixture and lead to the generation of either eruptible high SiO_2 melt pockets [*Bachmann and Bergantz*, 2003] or aplite and pegmatite veins [*London and Morgan*, 2012; *Thomas and Davidson*, 2013].

Therefore, in light of our reservoir scale simulations, we suggest that intrusive outgassing occurs via three stages controlled by different processes:

1. by discrete (non-connected) bubbles (ε_x≤0.4) that roughly accounts for a few % of the total amount of MVP outgassed;
2. by permeable outgassing via MVP channel formation (0.4≤ε_x≤0.7) that contributes to about 40-50% of the outgassing, and,
3. by capillary fracturing (ε_x>0.7), for the remaining of MVP loss.

The differences in style and rates between outgassing at low and high crystallinity will control the mass flux and composition of the magmatic gases released to the Earth's surface.

For instance, volatile species with a low solubility, or high compatibility with the MVP (e.g., S, Ar, N_2) are likely to partition into the MVP at low crystallinity and outgas predominantly during spikes of volcanic activity [*Shinohara*, 2013]. In contrast, less water-compatible or more soluble species (F, Br, and to some extent He) are expected to be dominantly released passively from intrusive bodies ("mush zones"; [e.g. *Paonita*, 2005]).

6. Conclusion

The multiscale modeling approach presented here allows us to shed light on the physical processes that control MVP outgassing in shallow silicic magmatic reservoirs. Our pore-scale numerical experiments at different Bond numbers (Bo=0.1-1 for mm-sized crystals), MVP and crystal volume fractions highlight the presence of a favorable crystal volume fraction window (0.4-0.7) where the buoyant MVP phase can overcome capillary forces and form MVP channels. We determine the critical MVP volume fraction for MVP channels to form as a function of crystal volume fraction. The pore-scale mechanics of bubble migration is then introduced as a parameterization in a thermo-mechanical magma reservoir model, which allows us (1) to compare directly outgassing efficiency over different ranges of crystal content in an evolving environment and (2) to constrain the role of the rheology of the surrounding crust on the mass balance of exsolved volatiles in the reservoir. This multiscale approach reveals that the size of the reservoir and visco-elastic response of the crust that surrounds it play a major role in the efficiency of intrusive outgassing. Large reservoirs and a hot crust (i.e. more prone to accommodate differential stresses viscously) allow for more substantial outgassing before the onset of capillary fracturing. Small reservoirs and/or colder crust (i.e. elastic stress response) are more prone to develop an adverse pressure gradient that favors a late-stage capillary fracturing mode of outgassing.

Under favorable conditions (viscous relaxation of the crust, Bo=0.5 and lithostatic pressure of 2 kbar), our simulations show that up to 40% of the initial water content of the magma can be released through MVP outgassing through MVP channels formation. Hence, other outgassing processes are needed to explain the very low residual water content of plutonic rocks in arcs. We suggest that at high crystal volume fraction (>0.7), ductile veining [*Weinberg and Regenauer-Lieb*, 2010] or capillary fracturing [*Holtzman et al.*, 2012; *Oppenheimer et al.*, 2015; *Shin and Santamarina*, 2010] may be viable process for MVP outgassing when magmas approach their solidus.

Appendix A. Lattice Boltzmann calculations

The lattice Boltzmann method (LBM) is a computational fluid dynamics technique that solves a discrete version of the Boltzmann equation [*Chopard et al.*, 2002]. LBM is well suited for dealing with complex multiphase fluids, and can be conveniently parallelized. These features allow LBM to be particularly efficient in modeling immiscible multiphase fluid flows in porous media [*Huber et al.*, 2013]. In order to take advantage of the parallel efficiency of LBM, we implemented the algorithm in an open-source parallel solver for LBM, Palabos (www.palabos.org) and performed our calculations on large computer cluster facilities (Dora at CSCS and Euler at ETHZ).

We perform our isothermal two-phase fluid flow pore-scale calculations with the color-gradient model (CGM) and a single relaxation time collision scheme that is based on *Leclaire et al.*, 2017. This CGM model allows us to deal with high viscosity ratios between the two immiscible fluids and explore a wider range of physical parameters compared to other lattice Boltzmann multiphase solvers [*Liu et al.*, 2016]. The CGM is well suited to deal with the competition between capillary, buoyancy and viscous stresses. This method was extensively tested against various benchmarks [*Leclaire et al.*, 2012].

The core algorithm of the color-gradient method is divided in six computational steps that are repeated at each time increment. We use the D3Q15 lattice since this cubic three-dimensional lattice offer the smallest computational workload [*Leclaire et al.*, 2017]. The probability distribution functions (PDFs) $N_i^k(\mathbf{x},t)$ and the indices *i*=(0,1,…13,14) and *k* are respectively related to the velocity space discretization and the "color" of the fluid (e.g. *k*=*r* for a red fluid and *k*=*b* for a blue fluid; for this manuscript, the red fluid is the MVP non-wetting phase (used index *g*), while blue one is the melt wetting phase (used index *m*)) describe the probability of finding a particle of fluid color *k* at position $\boldsymbol{x}$ and time *t*. In the CGM, the color-blind distribution function is important and for two-phase flow it is defined as

$$N_i(\mathbf{x},t) = N_i^r(\mathbf{x},t) + N_i^b(\mathbf{x},t) \qquad \text{A.1}$$

The first step consists of the color-blind single-relaxation-time lattice Boltzmann collision:

$$N_i^* = N_i - \omega_{eff}(N_i - N_i^e) + \Delta N_i \qquad \text{A.2}$$

where N_i^* is the distribution functions after the single-phase collision step. The quantity $\omega_{eff} = \frac{2}{6\nu+1}$ is the relaxation factor and is related to the effective kinematic viscosity of the fluids $\nu(\mathbf{x},\mathrm{t}) = \frac{\rho_r(x,t)\nu_r + \rho_b(x,t)\nu_b}{\rho_r(x,t) + \rho_b(x,t)}$, a density-weighted interpolation applied at the interface between the fluids to handle the desired viscosity contrast. ρ_k and $\nu_k = (1/3)(\tau_k - 0.5)$ are the density and kinematic viscosity for fluid k respectively; τ_k is the relaxation time for fluid k. The details of the equilibrium function N_i^e are given in *Leclaire et al.*, 2017, but essentially they depend on the local density $\rho_k(\boldsymbol{x},t)$ and velocity of the fluid $\mathbf{u}(\boldsymbol{x},t)$ as well as on the non-local color-blind density gradient $\nabla\rho(\mathbf{x},t)$. The local density and velocity of each fluid are obtained from the first and second moments of the distribution functions. The term ΔN_i allows us to add external forces, such as buoyancy force. The buoyancy of the MVP is introduced with ΔN_i = Bo (σ_{lu} / D_{lu}^2) $\boldsymbol{c}_{i,z}$ applied to the non-wetting fluid only [*Parmigiani et al.*, 2011], where Bo is the Bond number, σ_{lu} is the surface tension and D_{lu} the average diameter of the pore of the crystalline medium in lattice units (l.u) (see table 2).

The second step allows us to enforce the proper wetting conditions. Since the buoyant phase (MVP) is modeled as fully non-wetting, we can use the standard wetting boundary condition which uses ghost nodes and fictive density. This is done following the approach of *Leclaire et al.*, 2016.

The third step of the color-gradient method introduces interfacial tension effects at the interfaces between the immiscible fluids using a perturbation operator:

$$N_i^{**} = N_i^{*} + A|\mathbf{F}|\left(w_i \frac{(\mathbf{F}\cdot\boldsymbol{c}_i)^2}{|\mathbf{F}|^2} - B_i\right) \quad \text{A.3}$$

where the constant A is related to the strength of the interfacial force, and the weights w_i and B_i are lattice dependent weights [*Leclaire et al.*, 2017]. At last, the color gradient $\mathbf{F}$ is an approximation to the normal of the fluid-fluid interface:

$$\mathbf{F} = \nabla\left(\frac{\rho_r-\rho_b}{\rho_r+\rho_b}\right) \quad \text{A.4}$$

The perturbation operator introduces the capillary stress tensor back into the equations for immiscible two-phase flows [*Reis and Phillips*, 2007].

The fourth step is a recoloring operation, which is designed to preserve immiscibility while respecting mass and momentum conservation laws as well as controlling exactly the finite width of the interface [*Leclaire et al.*, 2015]:

$$N_i^{r,***} = \frac{\rho_r}{\rho} N_i^{**} + \beta\frac{\rho_r\rho_b}{\rho^2}\cos(\varphi_i)N_i^e(\rho,\mathbf{0}) \quad \text{A.5}$$

$$N_i^{b,***} = \frac{\rho_b}{\rho} N_i^{**} - \beta\frac{\rho_r\rho_b}{\rho^2}\cos(\varphi_i)N_i^e(\rho,\mathbf{0}) \quad \text{A.6}$$

where β is a parameter controlling the thickness of the numerical interface. In this study, we set β =0.7 (see Table 1) for an optimal trade-off of the interface thickness between the two immiscible fluids and the magnitude of the spurious velocities. The φ_i is the angle between the color gradient **F** and the lattice connectivity vector $\boldsymbol{c}_i$.

The fifth step is related to the solid-fluid boundary conditions for the distribution functions. The model we use here includes a solid-fluid no-slip boundary condition with the full-way bounce back approach [*Chopard et al.*, 2002], and finally, the sixth and last step is the usual lattice Boltzmann streaming step for each colored fluid.

Appendix B. Lumped parameter model for magma reservoir

The reservoir model of Degruyter and Huber [2014] solves the conservation of total mass (melt + crystals + volatiles), the conservation of water (most abundant magmatic volatile component), and enthalpy. The governing equations of the magma chamber model can be written in a condensed form as

$$\frac{dM}{dt} = \dot{M}_{in} - \dot{M}_{out} \qquad \text{(conservation of mass),} \qquad \text{B.1}$$

$$\frac{dM^w}{dt} = \dot{M}_{in}^w - \dot{M}_{out}^w \qquad \text{(conservation of water),} \qquad \text{B.2}$$

$$\frac{dH}{dt} = \dot{H}_{in} - \dot{H}_{out} \qquad \text{(conservation of enthalpy),} \qquad \text{B.3}$$

with M, M^w, and H the (total) mass, the water mass and the enthalpy of the magma chamber, respectively. The index "*in*" refers to source terms, while "*out*" indicates sink terms. We do not consider the injection of new magma and all the inflow terms are set to zero. There is also no mass loss due to eruptions and therefore the loss of mass reduces to outgassing $\dot{M}_{out} = \dot{M}_{out}^w = \dot{M}_{og}$ (the index *"og"* refers to MVP outgassing). The heat loss term $\dot{H}_{out} = \dot{Q}_{out} + \dot{H}_{pd}$, where $\dot{Q}_{out}$ represents the heat flow out of the magma chamber into the colder surrounding shell. This term is calculated using an analytical solution of an evolving temperature profile between a spherical magma chamber and a larger spherical shell with a radius ten times the initial radius of the magma chamber. The temperature of the outer shell is constant and set to the far-field temperature expected at the depth of the chamber (Table 2). The rheology of the surrounding shell is calculated according to the approach of *Dragoni and Magnanensi* [1989] and its effective viscosity is determined by the temperature profile in the crust. We thus can test the effect of crustal rheology on outgassing by varying the temperature at the boundary of the outer shell (Table 2). The mass and enthalpy loss rates during outgassing, ($\dot{M}_{og} = \rho_g \varepsilon_g U_{og} S$ and $\dot{H}_{og} = c_g T \dot{M}_{og}$) are calculated as follows:

- the MVP density ρ_g and the MVP volume fraction ε_g are obtained from the model,

- the surface area S is a constant in our calculations and is set to be a circular cross-section with a radius equal to the initial radius of the magma chamber,
- the MVP specific heat c_g is set to 3900 K/kg/K, [*Huber et al.*, 2010; *Lemmon et al.*, 2003]) and T is the average magma chamber temperature obtained from the model.
- the outgassing volume flux U_{og} is defined through closure expressions that we vary as a function of crystal and MVP volume fractions according to the results of the pore-scale simulations discussed in the main text.

For this, we divide the $(\varepsilon_m, \varepsilon_x, \varepsilon_g)$-space into four regions (Fig. 9), according to different possible outgassing mechanisms:

- $\varepsilon_g > 0.5$ (white region in Fig. 9): the MVP phase is the carrier phase. This condition is unlikely to be reached for realistic amounts of water at common storage depths. However, it can become relevant for magma ascent and fragmentation during explosive eruptions, which is beyond the scope of this study. The volume flux is not defined for this region.
- If $\varepsilon_g \leq 0.5$ and $\varepsilon_x < 0.4$ (blue region in Fig. 9): the MVP ascends as individual bubbles. The melt is the carrier phase and crystals cannot yet support a load. The volume flux U_{pd} is based on Stokes law for the ascent of an individual MVP bubble in a suspension [*Faroughi and Huber*, 2015; *Faroughi and Huber*, 2016]:

$$U_{og} = \frac{U^*(\rho_m - \rho_g) g r_b^2}{3\mu_{mx}} \tag{B.4}$$

with ρ_m, ρ_g the density of the melt and MVP phase calculated in the model; g = 9.81 m/s^2 the gravitational acceleration; r_b = 100 μm is the bubble radius; U^* the hindrance function related to the gas volume fraction ε_g:

$$U^* = \left(\frac{1-\varepsilon_g}{1-\frac{1}{2}\left(\frac{\varepsilon_g}{\psi_m}\right)}\right)\left(\frac{\psi_m - \varepsilon_g}{\psi_m(1-\varepsilon_g)}\right)^{\left(\frac{\psi_m}{1-\psi_m}\right)}\left(1 - \Upsilon\left(\frac{\varepsilon_g}{\psi_m}\right)^{\frac{1}{3}}\right) \tag{B.5}$$

with ψ_m = 0.637 the maximum random close packing fraction for mono-sized spherical particles and Υ=0.45 a geometrical constant derived from best fit value of experimental data for particles and drop suspensions experiments; μ_{mx} is the viscosity of the melt-crystal mixture:

$$\mu_{mx} = \mu_m \mu^* \tag{B.6}$$

with μ^* the hindrance function related to crystal volume fraction ε_x:

$$\mu^* = \left(\frac{\psi_m - \varepsilon_X}{\psi_m(1-\varepsilon_X)}\right)^{-2.5\left(\frac{\psi_m}{1-\psi_m}\right)}, \tag{B.7}$$

where μ_m is the viscosity of the melt is calculated using the parameterization of *Hess and Dingwell* [1996] for silicic melts:

$$\log_{10}\mu_m = \left[-3.545 + 0.833\ln\left(100m_{eq}\right)\right] + \frac{\left[9601 - 2368\ln\left(100m_{eq}\right)\right]}{\left[T - \left[195.7 + 32.35\ln\left(100m_{eq}\right)\right]\right]}, \qquad \text{B.8}$$

where m_{eq} is the dissolved water content in the melt and T the average temperature of the magma chamber (both evolving in the model).

- If $\varepsilon_g \leq 0.5$, $0.4 \leq \varepsilon_x < 0.7$, and $\varepsilon_g \geq \varepsilon_g^{cr}$ (black region in Fig. 9; equation (1)): outgassing can occur through connected MVP channels in a rigid crystal mush. The volume flux here is governed by a multiphase Darcy's law [*Paonita et al.*, 2016; *Weis et al.*, 2012]:

$$U_{og} = f_s \frac{k_r k}{\mu_g}\left(\frac{P - P_{lit}}{L} + \left(\rho_m - \rho_g\right)g\right) \qquad \text{B.9}$$

where the first term on the right hand side represents pressure driven flow with P the pressure of the magma body; P_{lit} is the lithostatic pressure set at 2 kbar; L is a characteristic length scale for the pressure-driven flow set to 100 m (which is equivalent to having a maximum under-pressure of a couple of MPa). The second term is the buoyancy force with ρ_m, ρ_g the density of the melt and gas phase and g = 9.81 m/s^2 the gravitational acceleration. k_r is the relative permeability defined in equation (3); k is the intrinsic permeability defined in equation (2), and the gas viscosity is set to μ_g = 6e^{-5} Pa s [*Lemmon et al.*, 2003]. f_s is an additional smoothing function to assure numerical stability across different outgassing regions:

$$\text{If } \varepsilon_g < \varepsilon_g^{cr} + 0.04,\ f_s = \left(\left(\varepsilon_g - \varepsilon_g^{cr}\right)/0.04\right)^4, \qquad \text{B.10}$$

$$\text{else, } f_s = 1.$$

- If $\varepsilon_x \geq 0.4$, and $\varepsilon_g < \varepsilon_g^{cr}$ (green region in Fig. 9; equation (1)): outgassing stops and U_{og} = 0 because there is not enough MVP to form/stabilize connected pathways. Bubbles remain trapped in the mush, and other processes such as capillary fracturing are necessary to promote further outgassing.

This set of equations closes the governing equations, which we solve using the ode15s subroutine in Matlab [*Shampine and Reichelt*, 1997], which is particularly well suited for stiff ordinary differential equations. We performed several reservoir calculations using the parameters and initial conditions reported in Table 2. The initial volume was varied to test the effect of a changing reservoir size on outgassing efficiency. All other model parameters are set to default values defined in *Degruyter and Huber* [2014].

Acknowledgements

A.P. and O.B. acknowledge support from the Swiss National Science Foundation (Ambizione grant no. 154854 to A.P., and project no. 200020-165501 to O.B.). C.H. was funded by a NSF CAREER grant (NSF EAR 1454821). S.L. thanks the FRQNT "Fonds de recherche du Québec – Nature et technologies" for financial support (research scholarship no. 183583). The simulations and cluster time was also supported by grants from the Swiss National Supercomputing Centre (CSCS) under the project s597, and the Euler Supercomputer from ETHZ. Data and scripts used for preparing most of the figures presented in this manuscript are available at https://sites.google.com/site/degruyterwim/perG3_data_graphs.zip. Lattice Boltzmann calculations were performed with the open-source PALABOS library (www.palabos.org) and we intend to make our CGM code available to the public under the same license soon (see also *Leclaire et al.*, 2017). The mathematical formulation and solution method of the magma reservoir model has been published in *Degruyter and Huber 2014*.

A.P. also thanks Dr. Benoit Lamy-Chappuis for discussion and careful revision of the manuscript and Vanni Tecchiato for his help with the handling of some figures.

FIGURES CAPTION:

Fig.1: Schematic representation of modelling approach for outgassing shallow reservoir (modified from Bachmann and Huber, 2016). We use a multiscale numerical approach to study the physics of outgassing in shallow magma reservoirs. At the pore-scale, we investigate the hydrodynamic conditions that allow MVP fingers to form by using a numerical isothermal pore-scale model for two-phase immiscible flows based on the lattice Boltzmann (LB) method. MVP bubbles (red) migrate because of their hydrostatic pressure drop (bubbles are buoyant) in a crystalline rigid environment (gray), coalesce and possibly form MVP fingers. Pore-scale results are then inserted as a parameterization into a thermomechanical magma reservoir model to provide a holistic view of the gas migration in cooling magma reservoirs.

Fig.2: Synthetic crystal-matrices and intrinsic permeability. a-d: Matrices at different crystal volume fractions produced with a crystal nucleation and growth algorithm similar to Avrami [1939] and modified by Hersum and Marsh [2006] that were used for our pore-scale calculations (size 160x160x240 l.u.). **e&f**: single fluid flow velocity field through crystalline matrix with ε_x=0.6 and ε_x=0.7 (magnitude in lattice units). Such calculations were used for intrinsic permeability estimation. **(g)** Estimated intrinsic permeability-k (logarithmic scale on y-axis) as a function of crystallinity and scaled to real units with an average crystal grain size of 4 mm [Cheadle et al., 2004]; see equation (2) for the expression of the 3rd order polynomial

fit. To show that the chosen matrix volume is a representative elementary volume we compare the intrinsic permeability obtained with a matrix of 160x160x240 l.u. with that of a larger matrix of 320x320x480 l.u., produced with the same algorithm. The two matrices sizes display very similar intrinsic permeability up to ε_x=0.7.

Fig. 3: Initial representative random MVP distribution (2^nd^ boiling scenario). Calculations for different MVP saturations ($S_g = \varepsilon_g/(1-\varepsilon_x)$) ($\varepsilon_g$ and ε_x are MVP and crystal volume fraction, respectively) defined as the pore volume fraction occupied by MVP, (S_g = **a)** 0.05, **b)** 0.1, **c)** 0.2, **d)** 0.3) equivalent to ε_g = 0.02, 0.04, 0.08, 0.12, respectively) in a crystal matrix with ε_x=0.6. Crystals and melt are transparent. At higher S_g, the effect of solid confinement on bubble shape is stronger.

Figure 4. MVP pore-scale calculations and channels formation. (a&b) MVP distribution and velocity field **(a&c)** before and **(b&d)** after MVP channels formation with Bo=0.5, ε_x=0.6 and ε_g=0.1 (crystalline matrix = gray, silicate melt = transparent). **e)** Occurrence of MVP channels (triangles) versus trapped or slow mobile MVP bubbles (circle). Continuous lines are MVP-saturation ($S_g = \varepsilon_g/(1-\varepsilon_x)$) contours, that quantifies the pore volume fraction occupied by the MVP. Dashed lines indicate ε_g under isobaric, closed-system, degassing (rhyolite-MELTS; Gualda et al. [2012]). **f)** Critical volume fraction of MVP at Bo=0.1, 0.5, 1. At ε_x=0.6 and Bo=0.1, our calculation shows that a MVP saturation higher than 0.4 has to be reached before MVP can flow through channels.

Fig. 5: MVP injection from below. **a)** Pore-scale calculation example for MVP fingering and channel formation at three different time snapshots for Bo= 0.5 and ε_x=0.6. h is the thickness of the inlet chamber that is occupied by the MVP only and determines the initial pressure drop which is responsible for winning the resistive capillary forces exerted by the porous medium (critical h for fingering to occur depends on capillary resistivity (i.e. crystal volume fraction) and Bo value). **b)** MVP-ε_g threshold for Bo=0.1, 0.5, 1 for ex-situ scenario.

Fig. 6: **Injection vs. 2^nd^ boiling-like channel formation, Bo=0.5.** MVP distribution and velocity field at the onset of channels formation for **a)** initial MVP random distribution (i.e. 2^nd^ boiling) and **b)** MVP injection from below at ε_x=0.6 and Bo=0.5.

Fig. 7: **Injection vs. 2^nd^ boiling-like channel formation, Bo=1.** MVP distribution and velocity field (magnitude in lattice units) at the onset of channels formation for **a)** MVP injection from below and **b)** initial MVP random distribution (i.e. 2^nd^ boiling) at ε_x=0.7 and Bo=1.

Fig. 8. MVP discharge and MVP relative permeability at the pore-scale. a) MVP Darcy volume flux U_{og}^{lu} (in lattice units l.u.) and **b)** relative permeability k_r for Bo=0.5. We report data only for calculations where MVP channels formed. Relative permeability is estimated from multiphase fluid flow Darcy's law $k_r = \frac{U_{og}^{lu}\nu_g}{k_{lu}(\Delta\rho g)_{lu}}$, where U_{og}^{lu} is the evaluated MVP volume flux (Fig. 8a) , ν_g the simulated MVP viscosity in l.u. and k_{lu} the intrinsic permeability as reported in Fig. 2g, but rescaled to l.u. (k_{lu} =$k/\Delta x^2$).

Figure 9. MVP transport: Modes of MVP transport in reservoir-scale model. The black area highlighted in red is based on pore-scale parametrization for MVP channel formation we obtained for Bo=0.5 (see eq.(1)).

Figure 10. Time evolution of crystal content in the reservoir model: calculations conducted to determine the effects on outgassing of (a) the temperature dependent visco-elastic rheology of the crust surrounding the chamber and (b) the initial size of the chamber. Time is normalized by the cooling time scale τ_c=R^2/κ, where R is the initial radius of the reservoir and the κ thermal diffusivity of the crust.

Figure 11. MVP transport at the reservoir scale: (a&c) total volatile mass fraction and **(b&d)** volatile mass fraction loss with respect to binned crystal volume fraction ε_x, for different crust viscosity (**a&b,** initial reservoir volume 50 km^3) and initial reservoir volume (**c&d**, crust viscosity 5x10^{17} Pa s). Black line = theoretical limit (perfectly viscous crust) where the loss of MVP is set by the critical MVP volume fraction. (**a&b)** As the crust viscosity increases, outgassing becomes limited by the pressure difference between the reservoir and the surrounding crust (see Fig. 12a&b). (**c&d)** In small reservoirs, the crust responds elastically to MVP loss, which impedes outgassing (see Fig. 12c&d). The gray area highlights crystal volume fraction above which MVP bubble migration and gas finger formation via capillary invasion is no-longer a viable mechanism for MVP outgassing.

Fig. 12 Thermomechanical chamber model: importance of the thermal state of the crust and chamber size: (a-c) Overpressure, and **(b-d)** MVP volume fraction for varying crust viscosity (**a-b**) and initial chamber volume (**c-d**). As in Fig. 11, the black line denotes the saturation limit. Pressure evolution in (a) during the reservoir scale calculations can be read as follow: (1) slow outgassing due to individual bubble rise; (2) rapid outgassing due to the presence of gas channels; (3) outgassing is hindered by the pressure drop in the chamber; (4) decrease in outgassing due to approach of MVP channel threshold with slight overshoot; (5)

outgassing is limited due to MVP channel threshold/saturation limit; (6) outgassing by gas channels ceases. Steps 4 and 5 only occur for a compliant crust and/or large chamber.

LIST OF TABLES:

Table 1. List of parameters used for pore-scale LB calculations based on the color gradient method (CGM). Physical parameters such as kinematic viscosity and surface tension are reported in lattice units (l.u.).

Table 2. Initial parameter choice for reservoir model calculations.

References

Anderson, A. T., G. H. Swihart, G. Artioli, and C. A. Geiger (1984), Segregation vesicles, gas filter-pressing, and igneous differentiation, *Journal of Geology*, *92*, 55-72.

Annen, C., J. D. Blundy, and R. S. J. Sparks (2006), The genesis of intermediate and silicic magmas in deep crustal hot zones, *Journal of Petrology*, *47*(3), 505-539.

Avrami, M. (1939), Kinetics of phase change. I General theory, *The Journal of Chemical Physics*, *7*(12), 1103-1112.

Bachmann, O., and G. W. Bergantz (2003), Rejuvenation of the Fish Canyon magma body: A window into the evolution of large-volume silicic magma systems, *Geology*, *31*(9), 789-792.

Bachmann, O., and G. W. Bergantz (2004), On the origin of crystal-poor rhyolites: Extracted from batholithic crystal mushes, *Journal of Petrology*, *45*(8), 1565-1582.

Bachmann, O., and G. W. Bergantz (2008), The Magma Reservoirs That Feed Supereruptions, *Elements*, *4*, 17-21.

Bachmann, O., and C. Huber (2016), Silicic magma reservoirs in the Earth's crust, *American Mineralogist*, *101*(11), 2377-2404.

Barker, G., and A. Mehta (1992), Vibrated powders: structure, correlations, and dynamics, *Physical Review A*, *45*(6), 3435.

Blundy, J., K. V. Cashman, A. Rust, and F. Witham (2010), A case for CO2-rich arc magmas, *Earth and Planetary Science Letters*, *290*(3-4), 289-301.

Boudreau, A. (2016), Bubble migration in a compacting crystal-liquid mush, *Contrib Mineral Petr*, *171*(4).

Candela, P. A. (1991), Physics of aqueous phase evolution in plutonic environments, *American Mineralogist*, *76*, 1081-1091.

Candela, P. A. (1994), Combined Chemical and Physical Model for Plutonic Devolatilization - a Non-Rayleigh Fractionation Algorithm, *Geochimica Et Cosmochimica Acta*, *58*(10), 2157-2167.

Candela, P. A. (1997), A review of shallow, ore-related granites: Textures, volatiles, and ore metals, *Journal of Petrology*, *38*(12), 1619-1633.

Caricchi, L., and J. Blundy (2015), Experimental petrology of monotonous intermediate magmas, *Geological Society, London, Special Publications*, *422*.

Cheadle, M., M. Elliott, and D. McKenzie (2004), Percolation threshold and permeability of crystallizing igneous rocks: The importance of textural equilibrium, *Geology*, *32*(9), 757-760.

Chelle-Michou, C., B. Rottier, L. Caricchi, and G. Simpson (2017), Tempo of magma degassing and the genesis of porphyry copper deposits, *Scientific Reports*, *7*, 40566.

Chopard, B., A. Dupuis, A. Masselot, and P. Luthi (2002), Cellular automata and lattice Boltzmann techniques: An approach to model and simulate complex systems, *Advances in complex systems*, *5*(02n03), 103-246.

Cooper, K. M., and A. J. R. Kent (2014), Rapid remobilization of magmatic crystals kept in cold storage, *Nature*, *506*(7489), 480-483.

Degruyter, W., and C. Huber (2014), A model for eruption frequency of upper crustal silicic magma chambers, *Earth and Planetary Science Letters*, *403*(0), 117-130.

Degruyter, W., A. Burgisser, O. Bachmann, and O. Malaspinas (2010), Synchrotron X-ray microtomography and lattice Boltzmann simulations of gas flow through volcanic pumices, *Geosphere*, *6*(5), 470-481.

Degruyter, W., C. Huber, O. Bachmann, K. M. Cooper, and A. J. R. Kent (2016), Magma reservoir response to transient recharge events: The case of Santorini volcano (Greece), *Geology*, *44*(1), 23-26.

Dragoni, M., and C. Magnanensi (1989), Displacement and Stress Produced by a Pressurized, Spherical Magma Chamber, Surrounded by a Viscoelastic Shell, *Phys Earth Planet In*, *56*(3-4), 316-328.

Edmonds, M., A. Brett, R. Herd, M. Humphreys, and A. Woods (2015), Magnetite-bubble aggregates at mixing interfaces in andesite magma bodies, *Geological Society, London, Special Publications*, *410*(1), 95-121.

Eriksen, F. K., R. Toussaint, K. J. Måløy, and E. G. Flekkøy (2015), Invasion patterns during two-phase flow in deformable porous media, *Frontiers in Physics*, *3*, 81.

Faroughi, S., and C. Huber (2015), Unifying the relative hindered velocity in suspensions and emulsions of nondeformable particles, *Geophysical research Letters*, *42*(1), 2014GL062570.

Faroughi, S., and C. Huber (2016), A predictive viscosity model for concentrated suspensions of rigid, randomly oriented spheroids, *accepted*.

Gardner, J. E., and M.-H. Denis (2004), Heterogeneous bubble nucleation on Fe-Ti oxide crystals in high-silica rhyolitic melts, *Geochimica et Cosmochimica Acta*, *68*(17), 3587-3597.

Gelman, S. E., F. J. Gutierrez, and O. Bachmann (2013), On the longevity of large upper crustal silicic magma reservoirs, *Geology*, *41*(7), 759-762.

Gerlach, T. M. (1991), Present-day CO2 emissions from volcanos, *Eos, Transactions American Geophysical Union*, *72*(23), 249-255.

Gualda, G. A. R., M. S. Ghiorso, R. V. Lemons, and T. L. Carley (2012), Rhyolite-MELTS: A modified calibration of MELTS optimized for silica-rich, fluid-bearing magmatic systems, *Journal of Petrology*, *53*(5), 875-890.

Gutierrez, F., I. Payacan, S. E. Gelman, O. Bachmann, and M. A. Parada (2013), Late-stage magma flow in a shallow felsic reservoir: Merging the anisotropy of magnetic susceptibility record with numerical simulations in La Gloria Pluton, central Chile, *Journal of Geophysical Research-Solid Earth*, *118*(5), 1984-1998.

Hammer, J. E. (2004), Crystal nucleation in hydrous rhyolite: Experimental data applied to classical theory, *American Mineralogist*, *89*(11-12), 1673-1679.

Heinrich, C. A., and P. A. Candela (2012), Fluids and Ore Formation in the Earth's Crust, *Treatise on Geochemistry, ed. 2*, *13*, 1-28.

Hersum, T. G., and B. D. Marsh (2006), Igneous microstructures from kinetic models of crystallization, *Journal of Volcanology and Geothermal Research*, *154*(1-2), 34-47.

Hess, K. U., and D. B. Dingwell (1996), Viscosities of hydrous leucogranitic melts: A non-Arrhenian model, *American Mineralogist*, *81*(9-10), 1297-1300.

Hildreth, W. S. (2004), Volcanological perspectives on Long Valley, Mammoth Mountain, and Mono Craters: several contiguous but discrete systems, *Journal of Volcanology and Geothermal Research*, *136*(3-4), 169-198.

Hinedi, Z., A. Chang, M. Anderson, and D. Borchardt (1997), Quantification of microporosity by nuclear magnetic resonance relaxation of water imbibed in porous media, *Water Resources Research*, *33*(12), 2697-2704.

Holtzman, R., M. L. Szulczewski, and R. Juanes (2012), Capillary fracturing in granular media, *Physical review letters*, *108*(26), 264504.

Huber, O. Bachmann, and M. Manga (2009), Homogenization processes in silicic magma chambers by stirring and mushification (latent heat buffering), *Earth and Planetary Science Letters*, *283*(1-4), 38-47.

Huber, Bachmann, and Manga (2010), Two Competing Effects of Volatiles on Heat Transfer in Crystal-rich Magmas: Thermal Insulation vs Defrosting, *Journal of Petrology*, *51*(4), 847-867.

Huber, O. Bachmann, J. L. Vigneresse, J. Dufek, and A. Parmigiani (2012), A physical model for metal extraction and transport in shallow magmatic systems, *Geochemistry Geophysics Geosystems*, *13, Q08003, doi:10.1029/2012GC004042*.

Huber, C., A. Parmigiani, J. Latt, and J. Dufek (2013), Channelization of buoyant nonwetting fluids in saturated porous media, *Water Resources Research*, *49*, 6371-6380.

Huybers, P., and C. Langmuir (2009), Feedback between deglaciation, volcanism, and atmospheric CO 2, *Earth and Planetary Science Letters*, *286*(3), 479-491.

Iacovino, K., et al. (2016), Quantifying gas emissions from the “Millennium Eruption” of Paektu volcano, Democratic People’s Republic of Korea/China, *Science Advances*, *2*(11).

Karakas, O., and J. Dufek (2015), Melt evolution and residence in extending crust: Thermal modeling of the crust and crustal magmas, *Earth and Planetary Science Letters*, *425*(0), 131-144.

Karakas, O., W. Degruyter, O. Bachmann, and J. Dufek (2017), Lifetime and size of shallow magma bodies controlled by crustal-scale magmatism, *Nature Geosci*, *advance online publication*.

Leclaire, A. Parmigiani, O. Malaspinas, B. Chopard, and J. Latt (2017), Generalized three-dimensional lattice Boltzmann color-gradient method for immiscible two-phase pore-scale imbibition and drainage in porous media *Physical Review E, 95(3), 033306.*

Leclaire, S., M. Reggio, and J.-Y. Trépanier (2012), Numerical evaluation of two recoloring operators for an immiscible two-phase flow lattice Boltzmann model, *Applied Mathematical Modelling*, *36*(5), 2237-2252.

Leclaire, S., N. Pellerin, M. Reggio, and J. Y. Trépanier (2015), An approach to control the spurious currents in a multiphase lattice Boltzmann method and to improve the implementation of initial condition, *International Journal for Numerical Methods in Fluids*, *77*(12), 732-746.

Leclaire, S., N. Pellerin, M. Reggio, and J.-Y. Trépanier (2016), A multiphase lattice Boltzmann method for simulating immiscible liquid-liquid interface dynamics, *Applied Mathematical Modelling*, *40*(13–14), 6376-6394.

Lee, C.-T. A., and D. M. Morton (2015), High silica granites: Terminal porosity and crystal settling in shallow magma chambers, *Earth and Planetary Science Letters*, *409*, 23-31.

Lemmon, E. W., M. O. McLinden, and D. G. Friend (2003), *Thermophysical Properties of Fluid Systems*, Gaithersburg MD, 20899.

Li, Y., Y. Xu, and C. Thornton (2005), A comparison of discrete element simulations and experiments for ‘sandpiles’ composed of spherical particles, *Powder Technology*, *160*(3), 219-228.

Lipman (2007), Incremental assembly and prolonged consolidation of Cordilleran magma chambers: Evidence from the Southern Rocky Mountain Volcanic Field, *Geosphere*, *3*(1), 1-29.

Lipman, P. W., and O. Bachmann (2015), Ignimbrites to batholiths: Integrating perspectives from geological, geophysical, and geochronological data, *Geosphere*.

Liu, H., Q. Kang, C. R. Leonardi, S. Schmieschek, A. Narváez, B. D. Jones, J. R. Williams, A. J. Valocchi, and J. Harting (2016), Multiphase lattice Boltzmann simulations for porous media applications, *Computational Geosciences*, 1-29.

London, D., and G. B. Morgan (2012), The pegmatite puzzle, *Elements*, *8*(4), 263-268.

Mangan, M., and T. W. Sisson (2005), Evolution of melt-vapor surface tension in silicic volcanic systems: Experiments with hydrous melts, *J. geophys. Res.*, *110, B01202, doi:10.1029/2004JB003215*.

Marsh (1989), Magma chambers, *Annual Review of Earth and Planetary Sciences*, *17*, 439-474.

Marsh, B. D. (1981), On the crystallinity, probability of occurrence, and rheology of lava and magma, *Contrib Mineral Petr*, *78*, 85-98.

Menand, T., C. Annen, and M. de Saint Blanquat (2015), Rates of magma transfer in the crust: Insights into magma reservoir recharge and pluton growth, *Geology*, *43*(3), 199-202.

Miller, C. F., D. J. Furbish, B. A. Walker, L. L. Claiborne, G. C. Koteas, H. A. Bleick, and J. S. Miller (2011), Growth of plutons by incremental emplacement of sheets in crystal-rich host: Evidence from Miocene intrusions of the Colorado River region, Nevada, USA, *Tectonophysics*, *500*(1-4), 65-77.

Mungall, J. E. (2015), Physical Controls of Nucleation, Growth and Migration of Vapor Bubbles in Partially Molten Cumulates, 331-377.

Navon, O., and V. Lyakhovsky (1998), Vesiculation processes in silicic magmas, in *The physics of volcanic eruptions*, edited by J. S. Gilbert and R. S. J. Sparks, pp. 27-50, Geological Society, London.

Ngachin, M., R. G. Galdamez, S. Gokaltun, and M. C. Sukop (2015), Lattice Boltzmann simulation of rising bubble dynamics using an effective buoyancy method, *International Journal of Modern Physics C*, *26*(03), 1550031.

Oppenheimer, J., A. Rust, K. Cashman, and B. Sandnes (2015), Gas migration regimes and outgassing in particle-rich suspensions, *Front. Phys. 3: 60. doi: 10.3389/fphy*.

Paonita, A. (2005), Noble gas solubility in silicate melts: a review of experimentation and theory, and implications regarding magma degassing processes, *Annals of Geophysics*.

Paonita, A., A. Caracausi, M. Martelli, and A. L. Rizzo (2016), Temporal variations of helium isotopes in volcanic gases quantify pre-eruptive refill and pressurization in magma reservoirs: The Mount Etna case, *Geology*, *44*(7), 499-502.

Parmigiani, A., C. Huber, and O. Bachmann (2014), Mush microphysics and the reactivation of crystal-rich magma reservoirs, *Journal of Geophysical Research: Solid Earth*, *119*(8), 6308-6322.

Parmigiani, A., C. Huber, O. Bachmann, and B. Chopard (2011), Pore-scale mass and reactant transport in multiphase porous media flows, *Journal of Fluid Mechanics*, *686*, 40-76.

Parmigiani, A., S. Faroughi, C. Huber, O. Bachmann, and Y. Su (2016), Bubble accumulation and its role in the evolution of magma reservoirs in the upper crust, *Nature*, *532*(7600), 492-495.

Pistone, M., et al. (2015), Gas-driven filter pressing in magmas: Insights into in-situ melt segregation from crystal mushes, *Geology*, *43*(8), 699-702.

Plank, T., K. A. Kelley, M. M. Zimmer, E. H. Hauri, and P. J. Wallace (2013), Why do mafic arc magmas contain ~ 4 wt% water on average?, *Earth and Planetary Science Letters*, *364*(0), 168-179.

Reis, T., and T. Phillips (2007), Lattice Boltzmann model for simulating immiscible two-phase flows, *Journal of Physics A: Mathematical and Theoretical*, *40*(14), 4033.

Ren, F., B. Song, and M. C. Sukop (2016), Terminal shape and velocity of a rising bubble by phase-field-based incompressible Lattice Boltzmann model, *Advances in Water Resources*, *97*, 100-109.

Shampine, L. F., and M. W. Reichelt (1997), The matlab ode suite, *SIAM journal on scientific computing*, *18*(1), 1-22.

Shin, H., and J. C. Santamarina (2010), Fluid-driven fractures in uncemented sediments: Underlying particle-level processes, *Earth and Planetary Science Letters*, *299*(1–2), 180-189.

Shinohara (2008), Excess degassing from volcanoes and its role on eruptive and intrusive activity, *Reviews of Geophysics*, *46, RG4005*.

Shinohara (2013), Volatile flux from subduction zone volcanoes: Insights from a detailed evaluation of the fluxes from volcanoes in Japan, *Journal of Volcanology and Geothermal Research*, *268*, 46-63.

Sillitoe, R. H. (2010), Porphyry Copper Systems, *Economic Geology*, *105*(1), 3-41.

Sisson, T. W., and C. R. Bacon (1999), Gas-driven filter pressing in magmas, *Geology*, *27*(7), 613-616.

Soden, B. J., R. T. Wetherald, G. L. Stenchikov, and A. Robock (2002), Global Cooling After the Eruption of Mount Pinatubo: A Test of Climate Feedback by Water Vapor, *Science*, *296*(5568), 727-730.

Spina, L., C. Cimarelli, B. Scheu, D. Di Genova, and D. B. Dingwell (2016), On the slow decompressive response of volatile- and crystal-bearing magmas: An analogue experimental investigation, *Earth and Planetary Science Letters*, *433*, 44-53.

Stöhr, M., and A. Khalili (2006), Dynamic regimes of buoyancy-affected two-phase flow in unconsolidated porous media, *Physical Review E*, *73*(3), 036301.

Thomas, R., and P. Davidson (2013), The missing link between granites and granitic pegmatites, *Journal of Geosciences*, *58*(2), 183.

Vidal, C. M., N. Métrich, J.-C. Komorowski, I. Pratomo, A. Michel, N. Kartadinata, V. Robert, and F. Lavigne (2016), The 1257 Samalas eruption (Lombok, Indonesia): the single greatest stratospheric gas release of the Common Era, *Scientific Reports*, *6*.

Wallace, P. J. (2005), Volatiles in subduction zone magmas: concentrations and fluxes based on melt inclusion and volcanic gas data, *Journal of Volcanology and Geothermal Research*, *140*(1-3), 217-240.

Ward, K. M., G. Zandt, S. L. Beck, D. H. Christensen, and H. McFarlin (2014), Seismic imaging of the magmatic underpinnings beneath the Altiplano-Puna volcanic complex from the joint inversion of surface wave dispersion and receiver functions, *Earth and Planetary Science Letters*, *404*(0), 43-53.

Weinberg, R. F. (1999), Mesoscale pervasive felsic magma migration: alternatives to dyking, *Lithos*, *46*(3), 393-410.

Weinberg, R. F., and K. Regenauer-Lieb (2010), Ductile fractures and magma migration from source, *Geology*, *38*(4), 363-366.

Weis, P., T. Driesner, and C. Heinrich (2012), Porphyry-copper ore shells form at stable pressure-temperature fronts within dynamic fluid plumes, *Science*, *338*(6114), 1613-1616.

Westrich, H. R., and T. M. Gerlach (1992), Magmatic gas source for the stratospheric SO2 cloud from the June 15,1991, eruption of Mount Pinatubo, *Geology*, *20*(10), 867-870.

White, S. M., J. A. Crisp, and F. A. Spera (2006), Long-term volumetric eruption rates and magma budgets, *Geochem. Geophys. Geosyst.*, *7*(doi:10.1029/2005GC001002).

Whitney, J. A. (1988), The origin of granite: The role and source of water in the evolution of granitic magmas, *Geological Society of America Bulletin*, *100*(12), 1886-1897.

Zellmer, G. F., M. Edmonds, and S. M. Straub (2015), Volatiles in subduction zone magmatism, *Geological Society, London, Special Publications*, *410*(1), 1-17.

Figure 1.

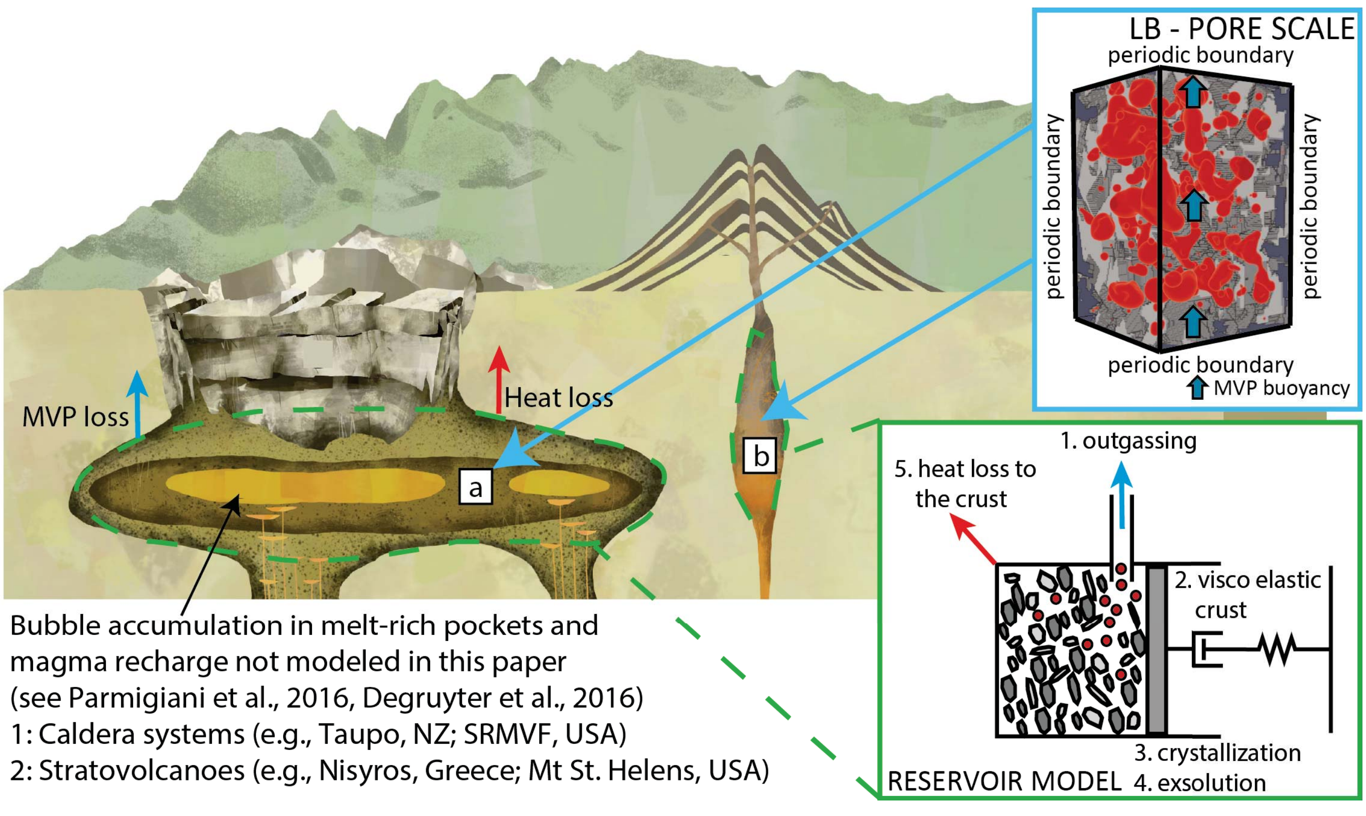
LB - PORE SCALE
periodic boundary
periodic boundary
periodic boundary
periodic boundary
MVP buoyancy
MVP loss
Heat loss
a
b
1. outgassing
5. heat loss to the crust
2. visco elastic crust
3. crystallization
4. exsolution
RESERVOIR MODEL
Bubble accumulation in melt-rich pockets and
magma recharge not modeled in this paper
(see Parmigiani et al., 2016, Degruyter et al., 2016)
1: Caldera systems (e.g., Taupo, NZ; SRMVF, USA)
2: Stratovolcanoes (e.g., Nisyros, Greece; Mt St. Helens, USA)

Figure 2.

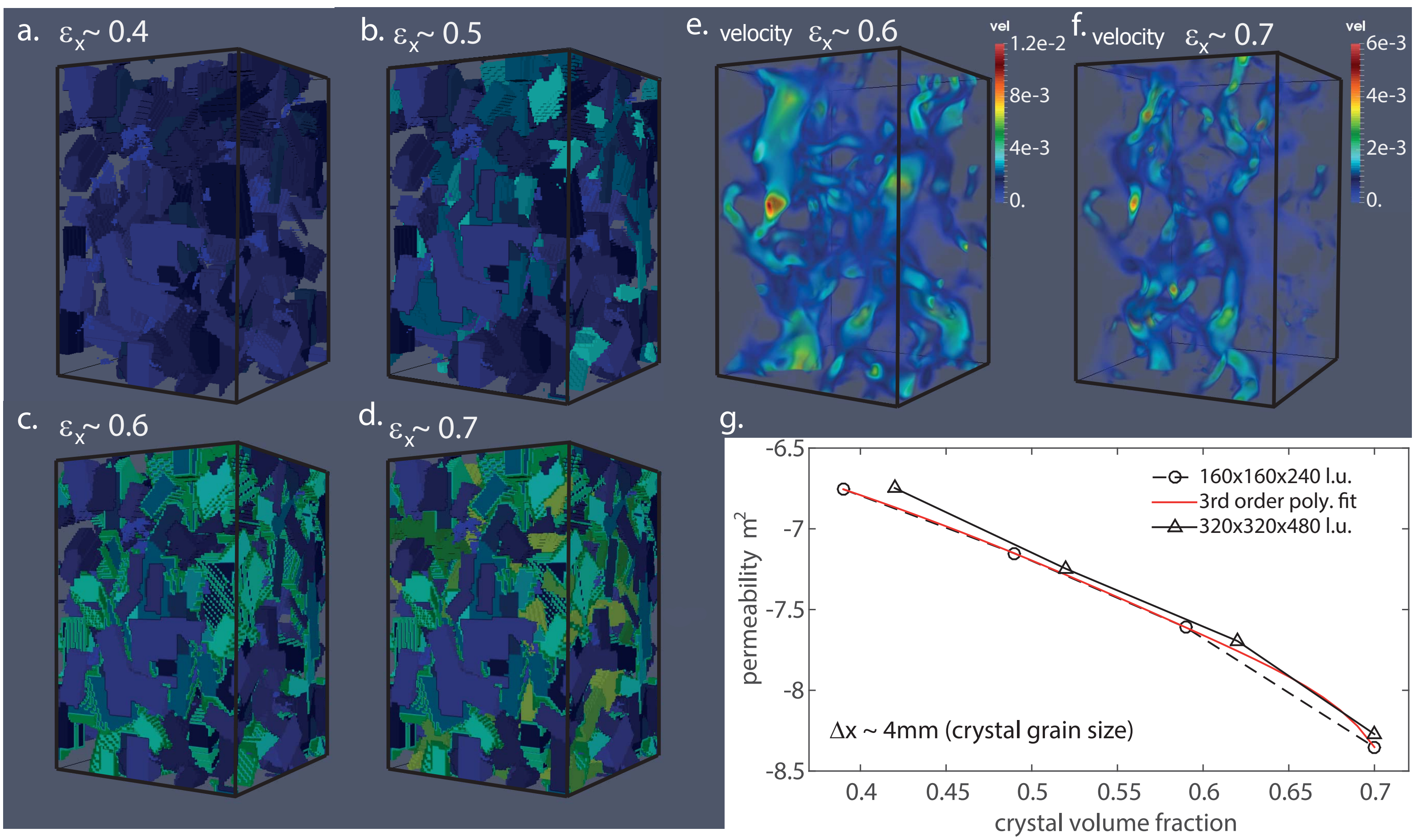

a. εx~ 0.4
b. εx~ 0.5
c. εx~ 0.6
d. εx~ 0.7
e. velocity εx~ 0.6
vel
1.2e-2
8e-3
4e-3
0.
f. velocity εx~ 0.7
vel
6e-3
4e-3
2e-3
0.
g.
permeability m²
crystal volume fraction
160x160x240 l.u.
3rd order poly. fit
320x320x480 l.u.
Δx ~ 4mm (crystal grain size)
-6.5
-7
-7.5
-8
-8.5
0.4
0.45
0.5
0.55
0.6
0.65
0.7

Figure 3.

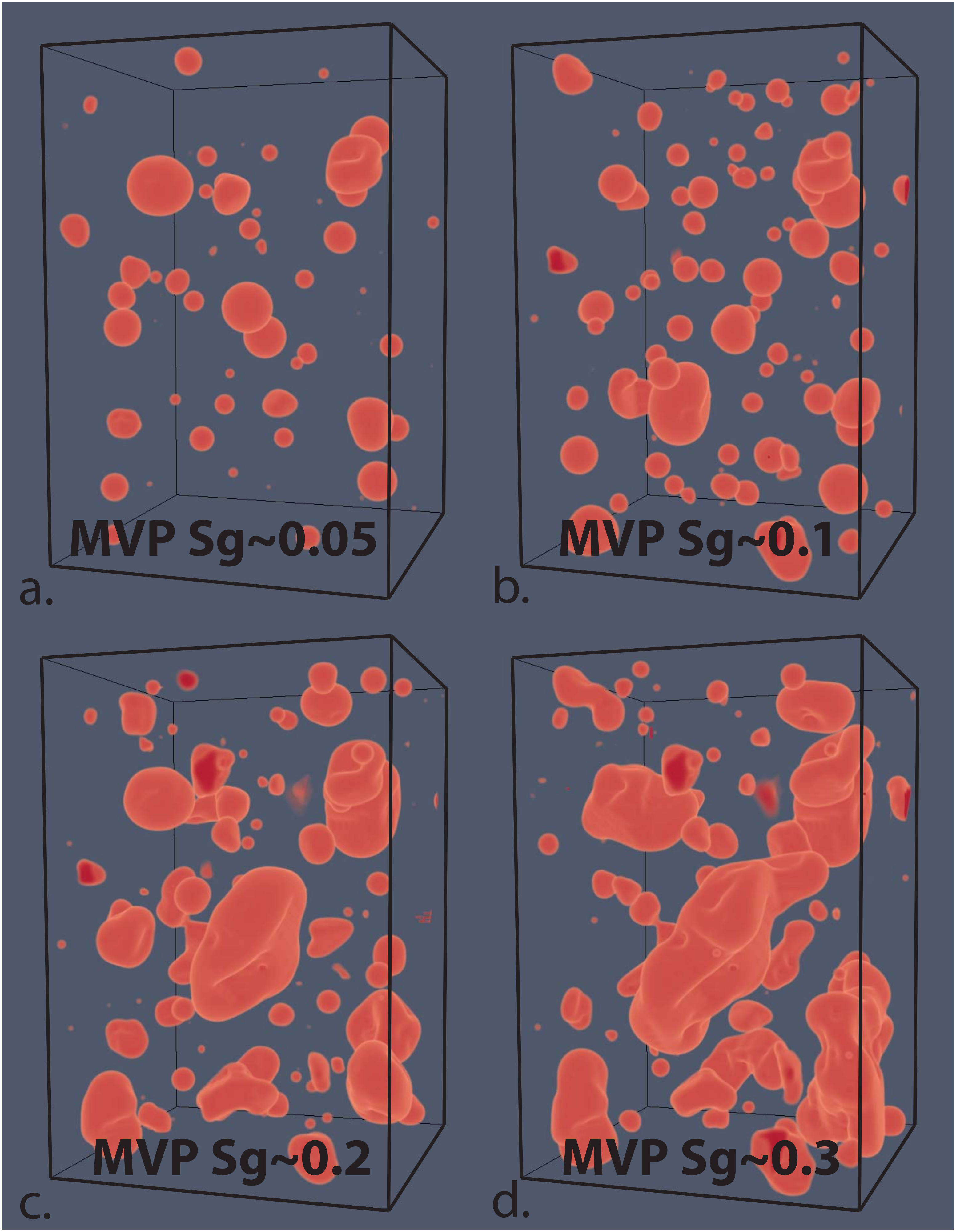

MVP Sg~0.05
a.
MVP Sg~0.1
b.
MVP Sg~0.2
c.
MVP Sg~0.3
d.

Figure 4.

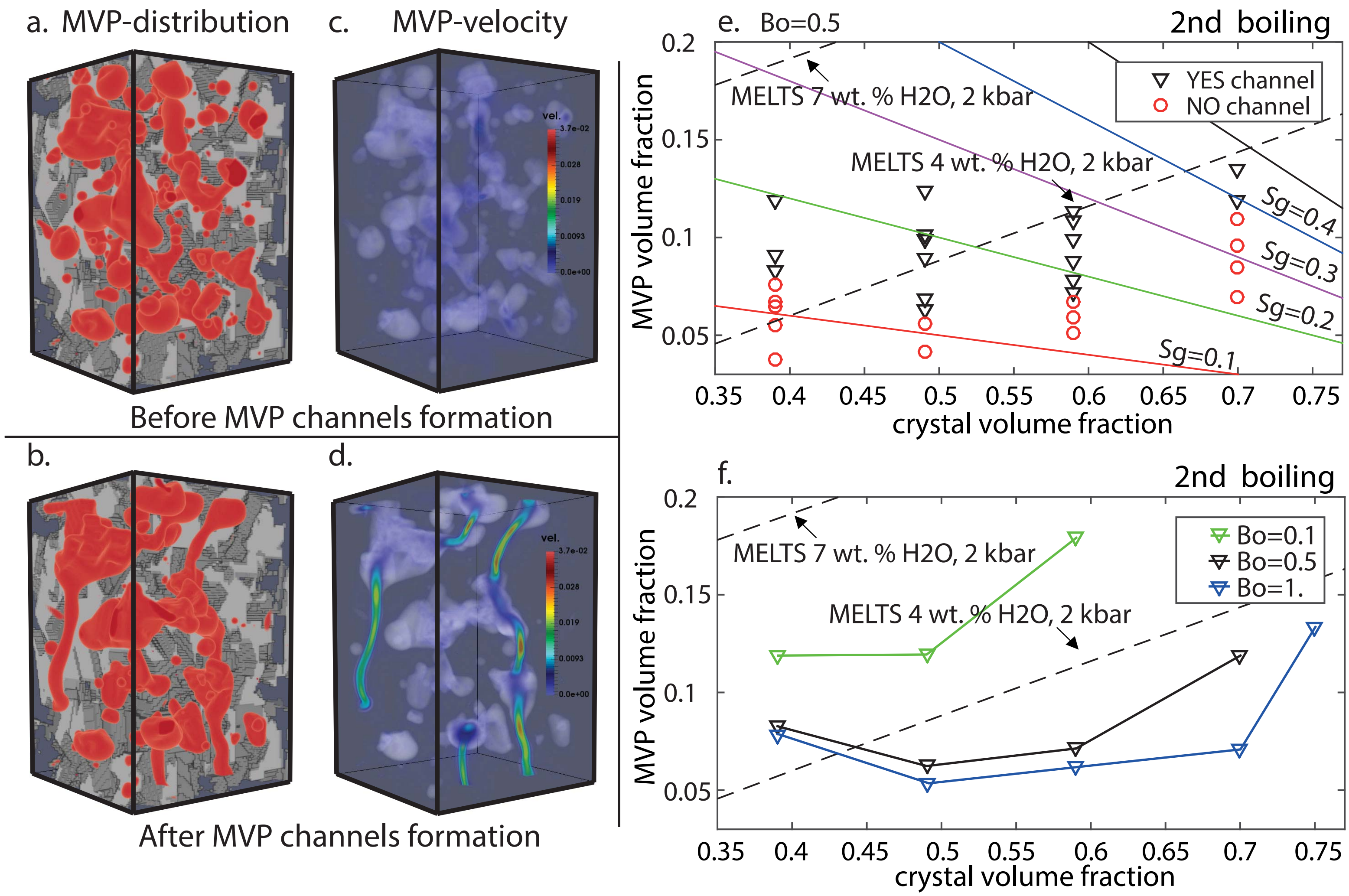

a. MVP-distribution
c. MVP-velocity
vel.
Before MVP channels formation
b.
d.
After MVP channels formation
e. Bo=0.5
2nd boiling
MVP volume fraction
crystal volume fraction
YES channel
NO channel
MELTS 7 wt. % H2O, 2 kbar
MELTS 4 wt. % H2O, 2 kbar
Sg=0.4
Sg=0.3
Sg=0.2
Sg=0.1
f.
2nd boiling
Bo=0.1
Bo=0.5
Bo=1.
MELTS 7 wt. % H2O, 2 kbar
MELTS 4 wt. % H2O, 2 kbar
MVP volume fraction
crystal volume fraction

Figure 5.

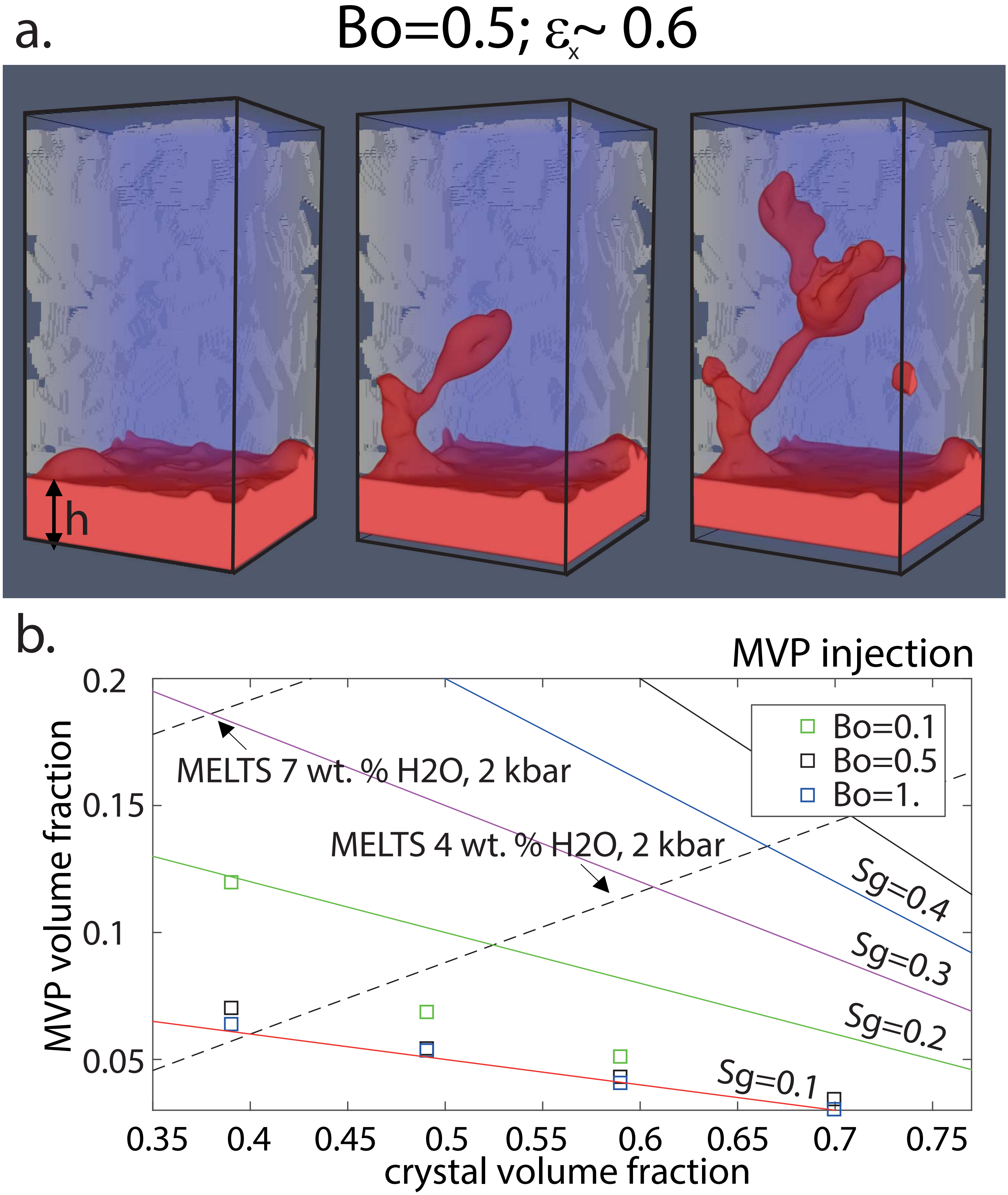
a.
Bo=0.5; ε_x~ 0.6
h
b.
MVP injection
MVP volume fraction
crystal volume fraction
Bo=0.1
Bo=0.5
Bo=1.
MELTS 7 wt. % H2O, 2 kbar
MELTS 4 wt. % H2O, 2 kbar
Sg=0.4
Sg=0.3
Sg=0.2
Sg=0.1
0.2
0.15
0.1
0.05
0.35
0.4
0.45
0.5
0.55
0.6
0.65
0.7
0.75

Figure 6.

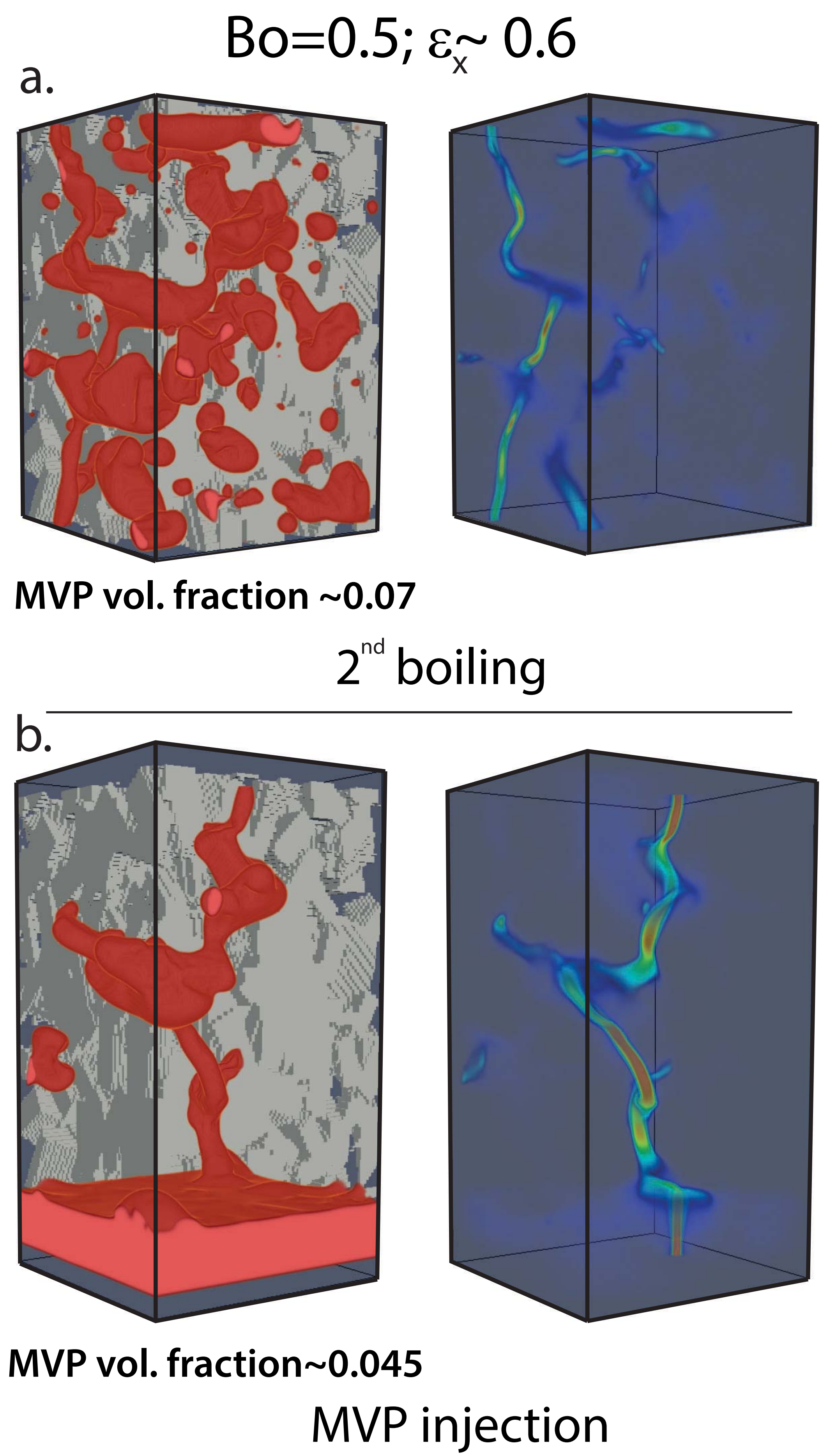
Bo=0.5; εx~ 0.6
a.
MVP vol. fraction ~0.07
2nd boiling
b.
MVP vol. fraction~0.045
MVP injection

Figure 7.

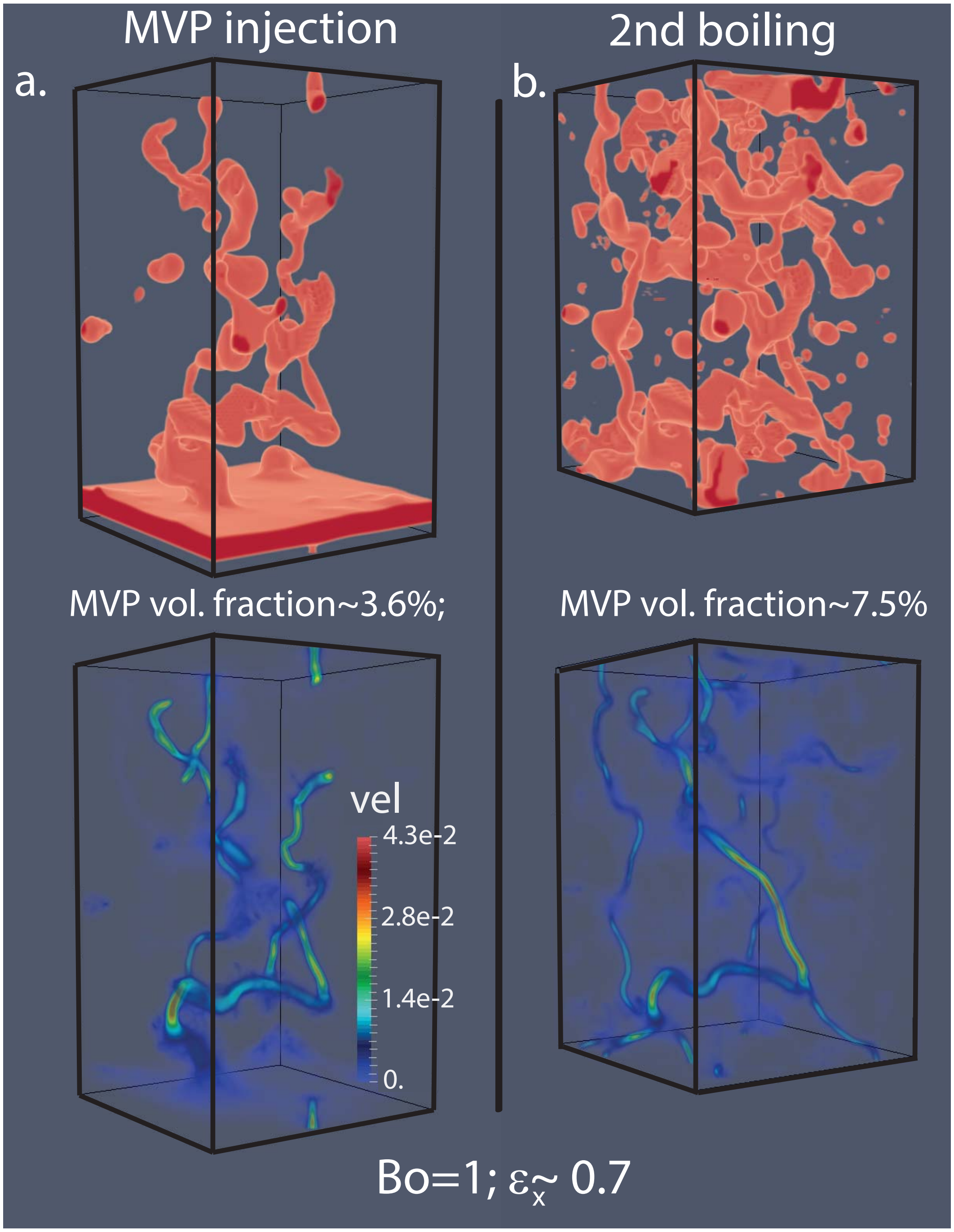
MVP injection
2nd boiling
a.
b.
MVP vol. fraction~3.6%;
MVP vol. fraction~7.5%
vel
4.3e-2
2.8e-2
1.4e-2
0.
Bo=1; ε_x~ 0.7

Figure 8.

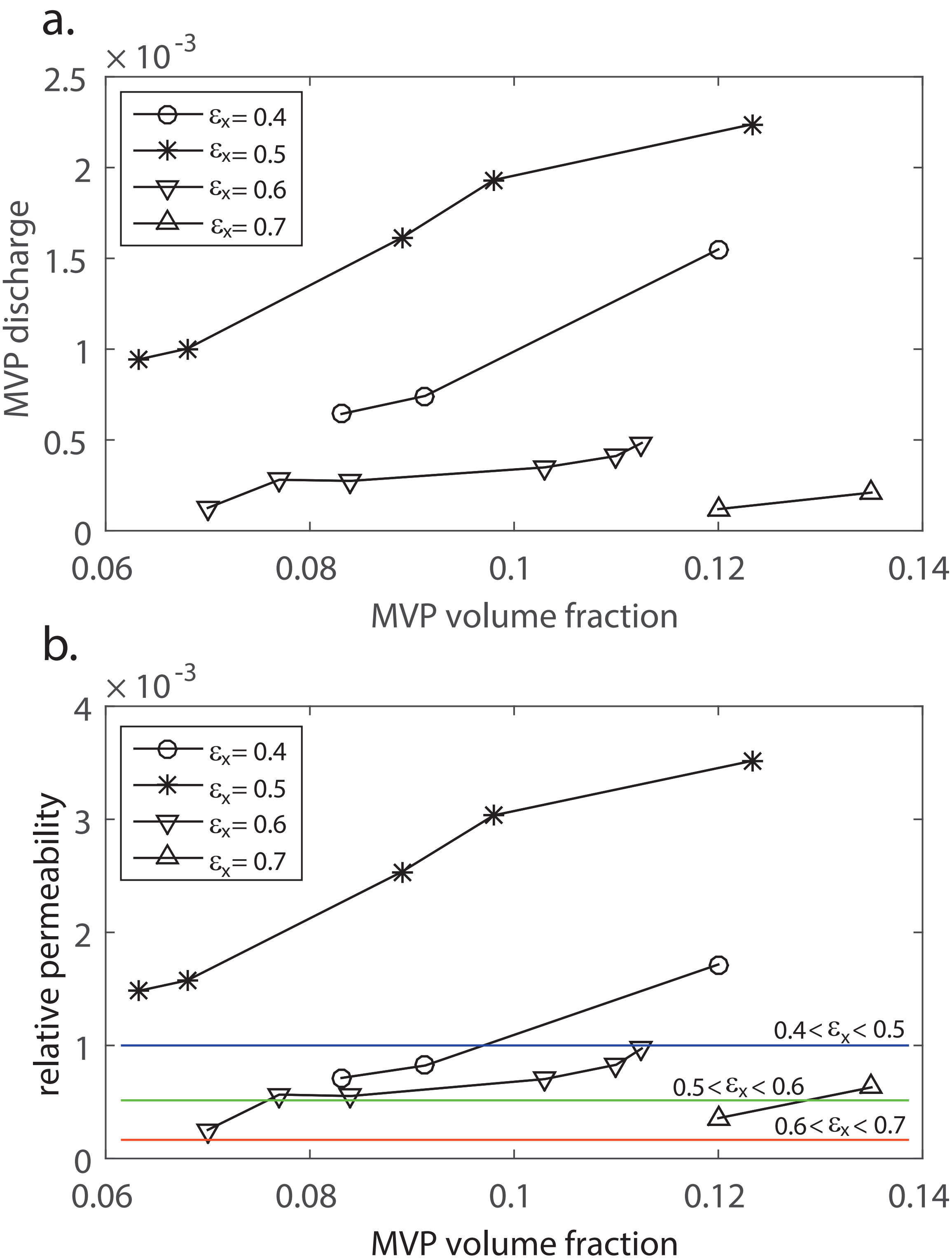

a.
× 10^-3
MVP discharge
MVP volume fraction
εx= 0.4
εx= 0.5
εx= 0.6
εx= 0.7
b.
× 10^-3
relative permeability
MVP volume fraction
εx= 0.4
εx= 0.5
εx= 0.6
εx= 0.7
0.4 < εx < 0.5
0.5 < εx < 0.6
0.6 < εx < 0.7

Figure 9.

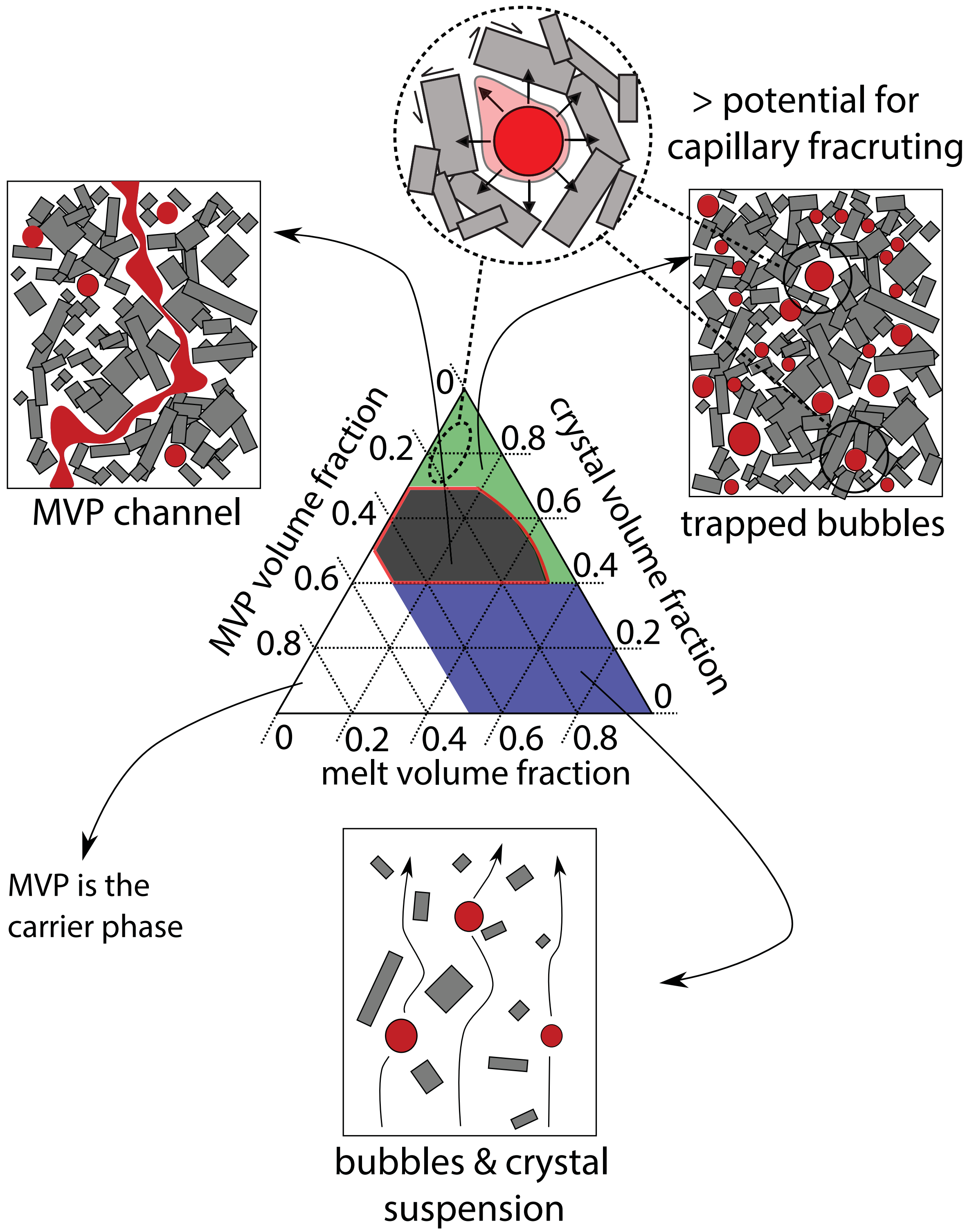

> potential for
capillary fracruting
MVP channel
trapped bubbles
0
0.2
0.4
0.6
0.8
MVP volume fraction
0.8
0.6
0.4
0.2
0
crystal volume fraction
0
0.2
0.4
0.6
0.8
melt volume fraction
MVP is the
carrier phase
bubbles & crystal
suspension

Figure 10.

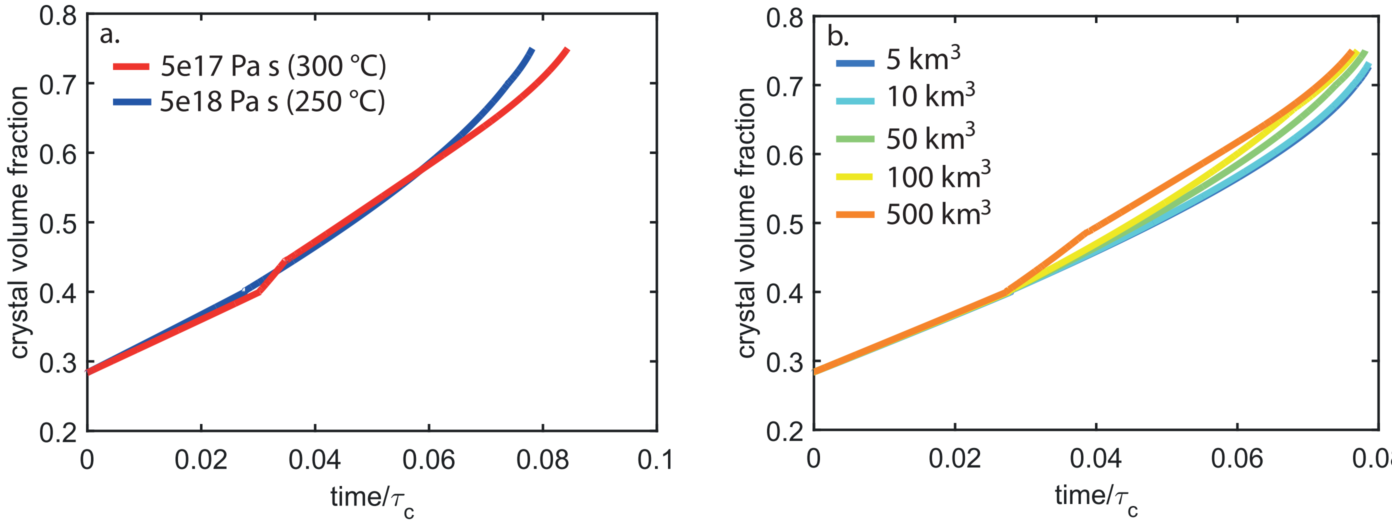
a.
5e17 Pa s (300 °C)
5e18 Pa s (250 °C)
crystal volume fraction
time/τ_c
b.
5 km^3
10 km^3
50 km^3
100 km^3
500 km^3
crystal volume fraction
time/τ_c

Figure 11.

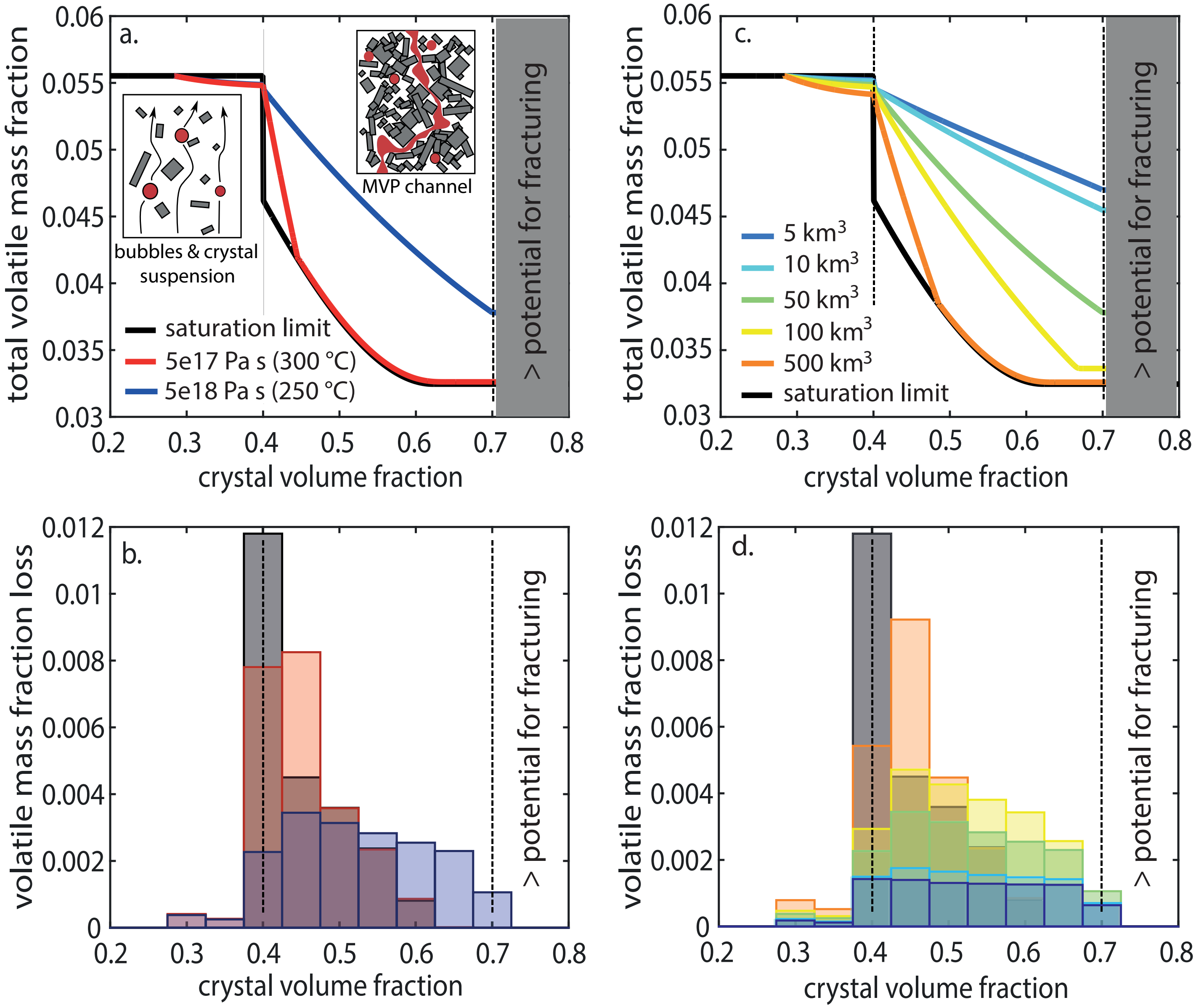
a.
bubbles & crystal suspension
MVP channel
saturation limit
5e17 Pa s (300 °C)
5e18 Pa s (250 °C)
> potential for fracturing
total volatile mass fraction
crystal volume fraction
b.
volatile mass fraction loss
c.
5 km^3
10 km^3
50 km^3
100 km^3
500 km^3
d.

Figure 12.

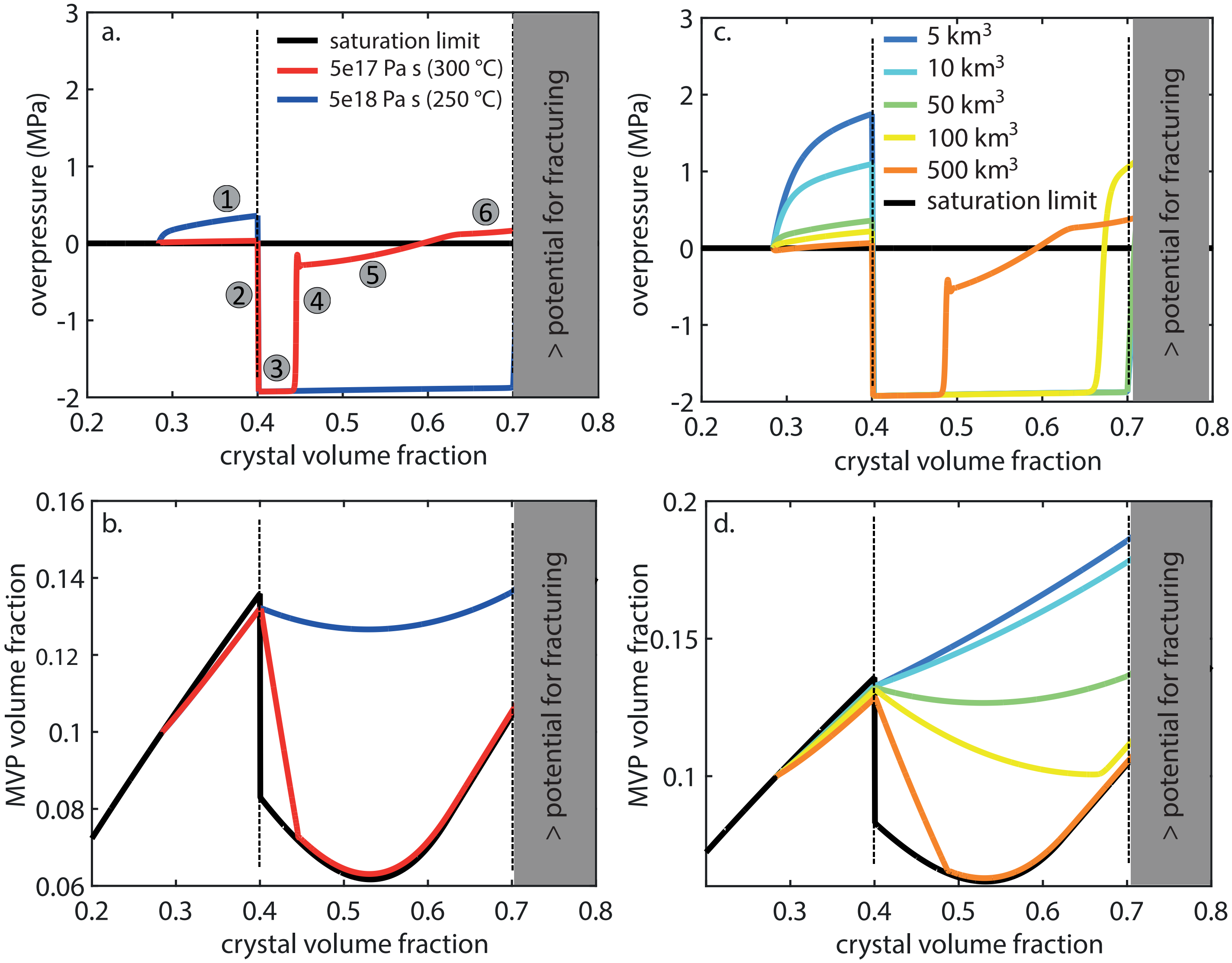
a.
saturation limit
5e17 Pa s (300 °C)
5e18 Pa s (250 °C)
overpressure (MPa)
crystal volume fraction
> potential for fracturing
1
2
3
4
5
6
b.
MVP volume fraction
crystal volume fraction
> potential for fracturing
c.
5 km3
10 km3
50 km3
100 km3
500 km3
saturation limit
overpressure (MPa)
crystal volume fraction
> potential for fracturing
d.
MVP volume fraction
crystal volume fraction
> potential for fracturing

symbol	Definition	Value
Bo	Bond number : $(g\Delta\rho)_{lu}\ D_{lu}^{2} / \sigma_{lu}$	0.1-1
$(g\Delta\rho)_{lu}$	body force-buoyancy in l.u. applied to MVP only	5e-6 - 5e-5
D_{lu}	average pore diameter in l.u.	10
σ_{lu}	surface tension in l.u.	5e-3
β	constant for thickness of diffuse interface	0.7
ε_x	crystal volume fraction	0.4 - 0.75
ε_g	MVP volume fraction	0.015 - 0.15
$\nu_b,\ \nu_m$	kinematic viscosity wetting phase ("melt") in l.u	0.5
τ_b	relaxation time for wetting phase	2
M	viscosity ratio: ν_r / ν_b	1/100
$\nu_r,\ \nu_g$	kinematic viscosity non-wetting phase ("MVP"): ν_bM	0.005
τ_r	relaxation time for non-wetting phase	0.515

Table 1

symbol	Definition	Value	Units
P_{lith}	lithostatic pressure	200	MPa
P_{ini}	initial chamber pressure	200	MPa
T_l	liquidus temperature	1020	°C
T_s	solidus temperature	700	°C
T_{ini}	initial chamber temperature	850	°C
T_c	temperature at the outer boundary of the visco-elastic crust	250-300	°C
∇T	geothermal gradient	~30	°C/km
b	power law exponent melting curve [*Huber et al.*, 2010]	0.5	
V_{ini}	initial chamber volume	5-500	km^3
M_{water}	initial fraction water mass content	5.6	wt %
η_{cold}	dynamic viscosity of the crust at T_c=250 °C	5.00e+17	Pa s
η_{hot}	dynamic viscosity of the crust at T_c=300 °C	5.00e+18	Pa s
κ	thermal diffusivity of the crust	1e-6	m^2/s
L_e	latent heat of exsolution [*Caricchi & Blundy*, 2015]	610e+3	J/Kg
L_m	latent heat of melting [*Caricchi & Blundy*, 2015]	290e+3	J/Kg

Table2